2017

Local Transient Characterization of Thermofluid Heat Transfer Coefficient at Solid-liquid Nano-interfaces

Mehrdad Mehrvand
University of Central Florida

LOCAL TRANSIENT CHARACTERIZATION OF THERMOFLUID HEAT TRANSFER COEFFICIENT AT SOLID-LIQUID NANO-INTERFACES

by

MEHRDAD MEHRVAND
M.S. University of Central Florida, 2015

A dissertation submitted in partial fulfillment of the requirements
for the degree of Doctor of Philosophy
in the Department of Mechanical and Aerospace Engineering
in the College of Engineering and Computer Science
at the University of Central Florida
Orlando, Florida

Summer Term
2017

Major Professor: Shawn A. Putnam

ABSTRACT

The demands for increasingly smaller, more capable, and higher power density technologies in microelectronics, energy, or aerospace systems have heightened the need for new methods to manage and characterize extreme heat fluxes (EHF). Microscale liquid cooling techniques are viewed as a promising solution for removing heat from high heat flux (HHF) systems. However, there have been challenges in physical understanding and predicting local thermal transport at the interface of micro and nanoscale structures/devices due to ballistic effects and complex coupling of mass, momentum, and energy transport at the solid-liquid-vapor interfaces over multiple time and length scales. Moreover, it's challenging to experimentally validate new HHF models due to lack of high resolution techniques and measurements.

This dissertation presents the use of a high spatiotemporal and temperature resolution measurement technique, called Time-domain Thermoreflectance (TDTR). TDTR is used to characterize the local heat transfer coefficient (HTC) of a water-cooled rectangular microchannel in a combined hot-spot heating and sub-cooled channel-flow configuration. Studies focused on room temperature, syringe-pumped single-and two-phase water flow in a ≈480 μm hydraulic diameter microchannel, where the TDTR pump heating laser induces local heat fluxes of ≈0.5-2.5 KW/cm^2 in the center of the microchannel on the surface of a 60-80 nm metal or alloy thin film transducer with hot-spot diameters of ≈7-10 μm.

In the single-phase part, a differential measurement approach is developed by applying anisotropic version of the TDTR to predict local HTC using the measured voltage ratio parameter, and then fitting data to a thermal model for layered materials and interfaces. It's shown that thermal effusivity distribution of the water coolant over the hot-spot is correlated to the local HTC, where both the stagnant fluid (i.e., conduction and natural convection) and flowing fluid (i.e., forced convection) contributions are decoupled from each other. Measurements of the local enhancement in the HTC over the hot-spot are in good agreement with established Nusselt number correlations. For example, flow cooling results using a Ti metal wall support a maximum HTC enhancement via forced convection of ≈1060±190 $kW/m^2 \cdot K$, where the well-established Nusselt number correlations predict ≈900±150 $kW/m^2 \cdot K$.

In the two-phase part, pump-probe beams are first used to construct the local pool and flow boiling curves at different heat fluxes and hot spot temperatures as a function of HTC enhancement. At a same heat flux level, it's observed that fluid flow enhances HTC by shifting heat transfer mechanism (or flow regime) from film boiling to nucleate boiling. Based on observations, it's hypothesized that beyond an EHF flow may reduce the bubble size and increase evaporation at the liquid-vapor interface on three-phase contact line, but it's unable to rewet and cool down the dry spot at the center due to the EHF.

In the last part of two-phase experiments, transient measurements are performed at a specific heat flux to obtain thermal temporal fluctuations and HTC of a single bubble boiling and nucleation during its ebullition cycle. The total laser power is chosen to be between the minimum required to start subcooled nucleation and CHF of the pool boiling.

This range is critical since within 10% change in heating flux, flow can have dramatic effect on HTC. Whenever the flow gets closer to the dry spot and passes through it (receding or advancing) HTC increases suddenly. This means that for very hot surfaces (or regions of wall dry-out), continuous and small bubbles on the order of thermal diffusion time and dry spot length scales respectively could be a reliable high heat flux cooling solution. This could be achieved by controlling the bubble size and frequency through geometry, surface structure and properties, and fluid's thermos-fluid properties.

To my family

ACKNOWLEDGMENTS

I would like to thank my advisor, Prof. Shawn Putnam, for his support, patience, and encouragement throughout my graduate studies at University of Central Florida. He introduced me to the interesting world of micro-and nano-scale heat transfer research and taught me a lot on this journey in theory and experiment whenever I needed. I appreciate all his contributions of time, ideas, technical, editorial and life advice.

I would also like to thank my committee members for their time, interest, and helpful comments. I used research results of Prof. Yoav Peles, as one of the pioneers in the heat transfer field frequently. Thank you Prof. Nina Orlovskaya for your help and letting me use chemicals in your lab. Prof. Reza Abdolvand, your great ideas and valuable assistances in the fabrication process of microchannels helped me a lot, thank you.

Special thanks to Dr. Joseph P. Feser (University of Delaware), John G. Jones (Air Force Research Lab), and Joshua Perlstein (University of Central Florida) for their gracious depositions of the NbV, Hf80, and Ti film coatings, respectively. Additionally, I must thank Kevin Gleason for his help on initial experiments setup. I must extend my gratitude to Mateo Gomez Gomez for his enthusiastic efforts in helping me during TDTR runs, and wish him greater achievements at Purdue University as a PhD student.

Thanks to all other members of the Interfacial Transport Lab, Alan Malmo, Richard Joshua Murdock, Harish Voota, Faraz Arya, Armando Arends, James Owens, Thomas Germain, Chance Brewer, Tanvir Chowdhury, and Krishnan Manhoran for the great talks and moments I have had with them during my graduate studies at UCF.

TABLE OF CONTENTS

LIST OF FIGURES

LIST OF TABLES

LIST OF ACRONYMS, ABBREVIATIONS, AND SYMBOLS

A = area of pump-laser hot-spot

C_p = volumetric heat capacity

$\mathcal{C}$ = constant

D_h = hydraulic diameter

D_{th} = thermal diffusivity

e_{th} = thermal effusivity

f_{mod} = modulation frequency

G = interfacial thermal conductance

G = mass flux

H = microchannel height

h = heat transfer coefficient (HTC)

h_0 = local HTC for a stagnant fluid

$h_{\uparrow}$ = local HTC enhancement (↑) due to forced convection

L = microchannel length

L_c = characteristic length-scale for heat transfer

ℓ_{th} = thermal penetration depth

Nu = Nusselt number

Nu_0 = local Nu for a stagnant fluid

$\mathrm{Nu}_{\uparrow}$ = local Nu enhancement (↑) due to forced convection

Pr = Prandtl number

$\tilde{P}_{\mathrm{laser}}$ = laser power converted into heat

q = heat flux

q_{CHF} = critical heat flux (CHF)

R = reflectance of the metal

Re_D = Reynolds number based on hydraulic diameter =

t_c = characteristic time-scale for heat transfer

T_{f} = fluid temperature

T_{f}^{∞} = fluid temperature at the microchannel inlet

T_{S} = surface/wall temperature

T_{HS} = hot spot temperature

V_{in} = in-phase TDTR voltage

V_{out} = out-of-phase TDTR voltage

$\frac{V_{in}}{V_{out}}$ = TDTR voltage ratio

$\vec{\mathrm{v}}_{\mathrm{avg}}$ = average fluid velocity

$\vec{\mathrm{v}}_{\mathrm{g}}$ = group velocity of TDTR thermal waves

$\vec{\mathrm{v}}_{\ell_{th}}$ = fluid velocity at a perpendicular depth ℓ_{th} from the hot-spot

$\vec{\mathrm{v}}_{\mathrm{max}}$ = maximum fluid velocity in the center of the microchannel

x = flow direction, distance from the microchannel inlet

W = microchannel width

w = beam waist, $1/e^2$ radius of the focused pump laser

z = perpendicular distance from the metal wall into the channel

Greek symbols

δ_h = thickness of the hydrodynamic boundary layer

δ_{th} = thickness of the thermal boundary layer

ΔT = temperature difference between the fluid and metal wall/surface

ΔT_{AC} = amplitude of the temperature oscillations in metal due to AC pump heating

Δx = pump-probe offset

$\Delta x/w$ = offset ratio

μ_∞ = dynamic viscosity of the fluid at the microchannel inlet

μ_{tBL} = dynamic viscosity of the fluid in the thermal BL

ν = kinematic viscosity

ω = angular heating frequency

τ_d = pump-probe time-delay

Λ = thermal conductivity

Acronyms

BL = boundary layer

fs = femtosecond

FS = fused silica

ktg = kinetic theory of gases

HTC = heat transfer coefficient

ROI = region of interest

CHAPTER 1: INTRODUCTION

1.1 Background and motivation

1.1.1 Microscale high heat flux devices

For decades, there has been great interest among industries in scaling down and shrinking their products' size due to different reasons such as less material, weight, and energy usage, smaller size, easier transportation and better portability, and final cost and market desire. For example, the semiconductor and microelectronics industry has benefited from continuous miniaturization evolution and power increase over the past four decades to reduce room-sized Mainframe computers to million times faster laptops or pocket-size cellphones. This evolution which has led to a new class of machines every 5-10 years (shown in Figure 1-1(a)) [1], has been enabled by shrinking of transistors as the fundamental building block down to 10-100 nm dimensions and placing 10-100 millions of them on a single chip or an Integrated Circuit (IC) in the recent years. This is ruled as Moore's law and states that the number of transistors on a microprocessor chip will double every two years as indicated in Figure 1-1(b).

We would be lucky if the increased functional density and reduced size and cost were the only consequences. However, overheating was a throwback to the miniaturization which began when the feature size reached the 90 nm limit and below in the early 2000s. The solution to this was to cap the processors' clock speed as it's shown

by the blue plateau area in the Figure 1-1(b) while increasing the number of chips by redesigned multi-core processors [1].

"High Heat Flux" (HHF) situation, which means relatively large amount of heat loads distributed or imposed over smaller areas [2], can be seen not only in microelectronics but in many of today's devices and technologies such as diode lasers, data centers, energy production and storage systems. Figure 1-1(b) outlines this growing challenge faced by the microelectronics industry for the next generations of devices [1], where, for example, the heat fluxes within the next decade are expected to surpass 3 KW/mm^2 which is nearly 50 times greater than the heat flux radiated by the Sun [3].

The heat dissipation in an IC is highly local with some high temperature and high

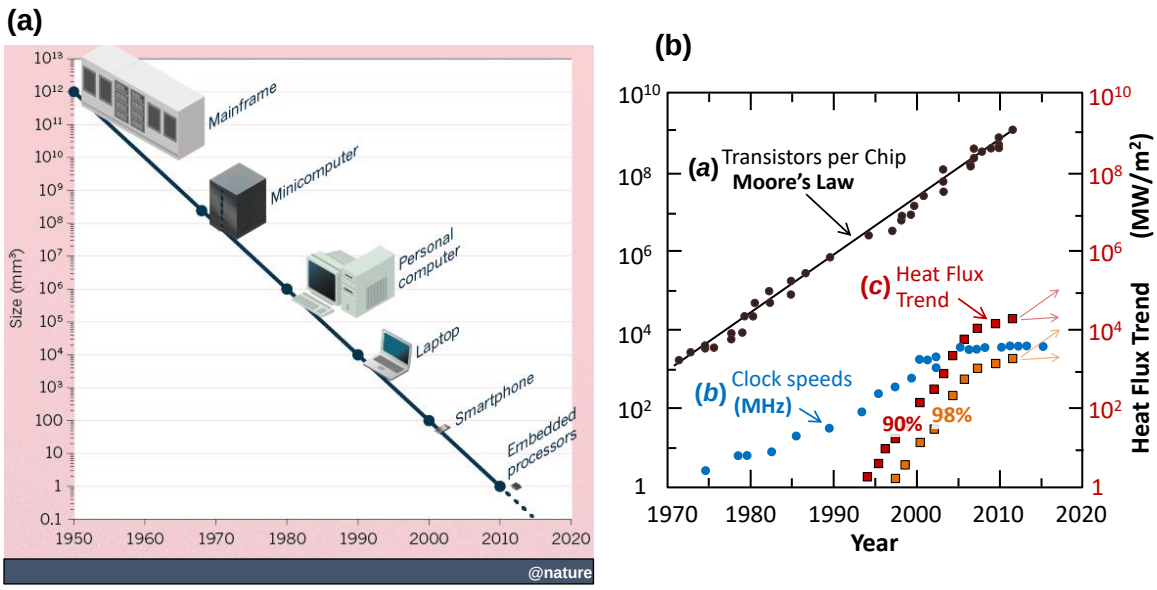

Figure 1-1 (a) Computer miniaturization evolution [1]. (b) Number of transistors per chip, Moore's law (black-line), microprocessor clock speeds (blue circles), hot-spot heat fluxes calculated via the transistor and clock-speed trends for a processor die area of 500 mm^2, DARPA's goal of 20 pJ per (fl)op, and (fl)op efficiencies of 90% and 98%.

heat flux points on the circuit which are known as “hot spots”. The greatest thermal challenges in microelectronics is in the packaging of processors not only due to the largest overall power dissipation, but because the hot spots [4]. According to the 2015 Technology Roadmap for Semiconductors [5], both average and local power densities will increase in the future designs. Performance and reliability of thermal solutions will be limited by transient hot spot thermal management even when the total and average power meets the design specification and requirements.

1.1.2 Thermal transport at nano-interfaces

Development of nano-devices in microelectronics, biomedical, or energy applications brings concerns about removal of the dissipated heat and thermal management at interfaces between nano-layers and other materials or mediums [6,7]. Since nano-structures or nano-devices have relatively less bulk material, thermal transport is dominated at their interfaces [7]. To understand this behavior let’s take a closer look at the thermal transport at interfaces. Figure 1-2 shows heat flow (q) from the box A (left) to the box B (right) and temperature distribution along the heat flow direction for three cases. In the first one there is an air gap at the interface due to surface roughness and imperfect contact. These air gaps and rough surfaces create a resistance to the heat flow which is called Thermal Contact Resistance (R_c) and it causes a temperature drop of $\Delta T_c = T_A - T_B$ from the surface A to the surface B across the interface. Contact resistance is macroscopic and important to bulk surfaces.

In Figure 1-2 (b) the contact surfaces of A and B are perfect with no roughness

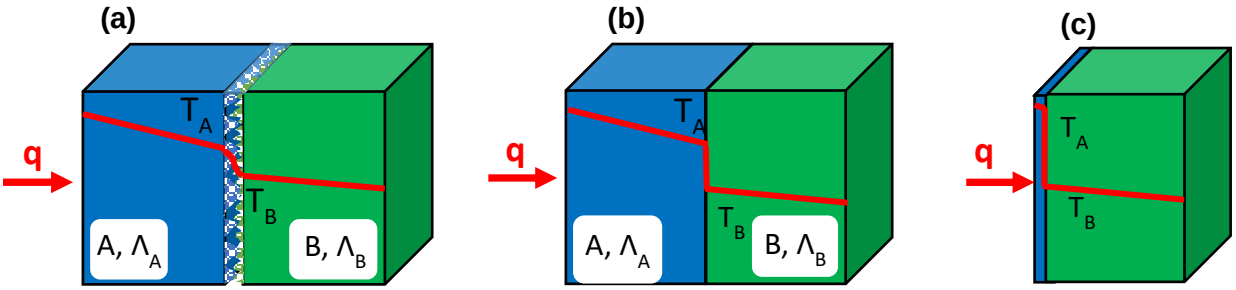

Figure 1-2 Heat flow across a (a) common bulk interface, (b) perfect and ideal bulk interface, and (c) nano-interface and temperature drop at the interface due to (a) contact resistance, (b) boundary resistance, and (c) nano-structure boundary resistance

and air gap between. Unlike the common sense of no resistance and temperature drop at this interface there is a resistance due to different acoustic (vibrational and electronic) properties of materials and surfaces of A and B which is called Thermal Boundary Resistance (R_b). It happens when an energy carrier (phonon or electron) scatters at interface while trying to crossover the interface. Boundary resistance is microscopic, present even at ideal contacts, and important to nano-structures and small scale devices. As it's illustrated in Figure 1-2 (c) when the box A is converted to a thin layer instead all the heat should flow through the thin layer and since there is less bulk material and surfaces the temperature drop of ΔT_b is more than (b).

Thermal boundary resistance (or inversely interfacial thermal conductance (G)) relates the heat flow q crossing the planar interface to the local temperature drop ΔT_b at the interface between two sides by this equation [8]:

$$q = \Delta \mathrm{T}/R_b = G\Delta \mathrm{T} \qquad (1\text{-}1)$$

Thermal interface conductance which has the $W/m^2.K$ unit, has a limited range at room temperature for balk materials interface compared to the other thermal properties

based on the interface composition at a molecular layer level [9] and is usually measured between 10 and 100 MW/m^2K [7,10–13] for practical materials and applications. For the physical meaning purpose, G can be interpreted as an equivalent thermal impedance or an equivalent thickness (d) of a dielectric layer by relating them to the thermal conductivity of dielectric ($G = \Lambda/d$). For example, an interface with a typical conductance of $G = 10^7 W/m^2K$ (or $R_b = 10^{-7} m^2K/W$) is equivalent to the thermal impedance of 140 nm of SiO_2 or 15 μm of Si.

As we know one or more of heat carriers (phonon, electron, or photon) and/or fluid particles (atoms or molecules) are present and dominant in any heat transport process depending on the material type, phase, and mode of heat transfer. The upper limit for interfacial thermal conductance of bulk materials belongs to high-conductivity-metals interfaces such as Al/Cu with electrons as dominant energy exchange carriers and the lower limit of G is at interfaces with highly mismatched phonon modes such as Bi/H-diamond [11].

Heat carriers or fluid particles have interactions with each other at interfaces such as phonon-phonon, phonon-electron or phonon-boundary scattering due to the differences in electronic and vibrational properties in different materials. When an energy carrier attempts to traverse the interface, it will scatter at the interface which makes heat transport at interfaces more difficult to predict.

In Figure 1-3 (b) a typical transistor with micro-size substrate and nano-size device layer is shown. In the left side (Figure 1-3 (a)) mean free paths of phonons in some common substrate materials are plotted as a function of temperature. It has been observed that length scale of the substrate or device determines heat transport

mechanism at any given temperature. For example, at room temperature heat transports diffusively within Si and SiC for dimensions above $\cong 550\ nm$ and $1.1\ \mu m$ respectively and ballistically or quasi-ballistically below those limits. Fourier diffusion law for macroscopic sizes fails when characteristic length of the device or the system is comparable to the mean free path of the heat carrier or when the time scale of the physical system is smaller than the relaxation time of the heat carriers.

All the above-mentioned issues imply that low thermal resistance or high conductance at interfaces is desirable for very high heat flux and dissipation applications. As expected by the International Technology Roadmap for Semiconductors this is vital to the development of microelectronic semiconductor devices where an 8 nm feature size device is projected to generate up to 100 kW/cm^2 and would need efficient heat dissipation of an anticipated die level heat flux of 1 kW/cm^2 which is an order of magnitude higher than current devices [14]. This means that interfaces are critical at the nanoscale.

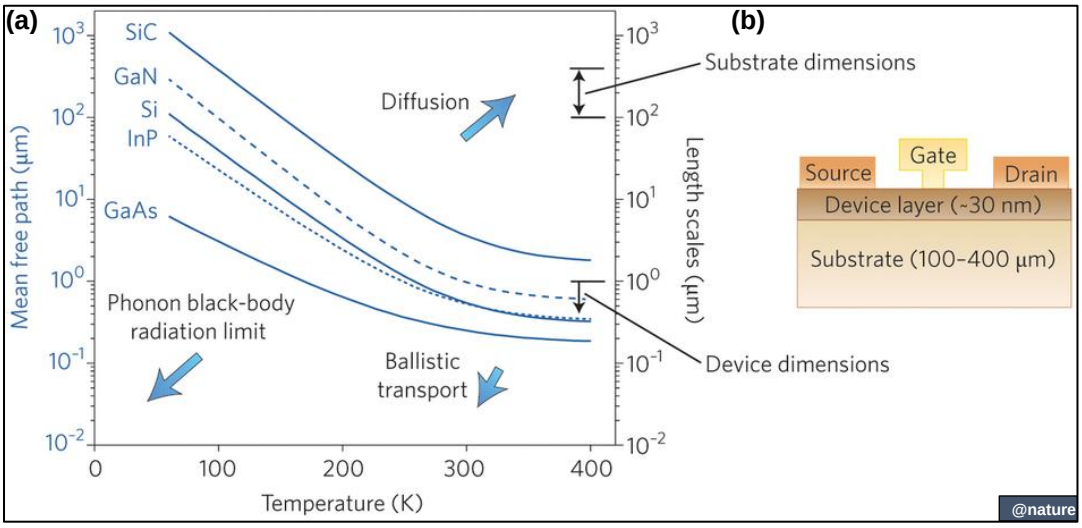

Figure 1-3 (a) Temperature dependence of the mean free paths of phonons in a variety of common substrate materials. (b) Typical transistor with nano-size device layer

1.2 Approach and outline

Microscale liquid cooling is a promising cooling method for high heat flux systems. Different forms of liquid cooling systems as spray cooling, jet impingement, immersion, heat pipes, mini and microchannels have been developed during the last two decades. Microchannels have been of particular interest for practical microscale cooling of HHF systems. Microchannel is used in this dissertation to study heat transport at its nano-size wall interface with liquid coolant using an optical and non-contact high resolution technique called Time-Domain Thermo-Reflectance (TDTR).

In the next chapter theories and literatures related to microscale cooling of HHF devices and TDTR method will be provided. Details about the experimental setup of sample stage, microchannel, and TDTR and the measurement methodology will be discussed in chapter CHAPTER 3:.

For proof of principle, single-phase water in rectangular microchannels and corresponding methodology for HTC analysis to decipher the thermo-fluid transport inside and outside the thermal BL will be studied in chapter CHAPTER 4:. This work also builds on past TDTR studies of droplet impingement and evaporation and facilitates later thermo-physical studies of multi-phase heat and mass transport in chapter CHAPTER 5:. Summary and future direction will be concluded in chapter CHAPTER 6:.

CHAPTER 2: THEORY AND LITERATURE

2.1 Introduction

Temperature control is a critical regulatory process in a wide variety of systems. Without it, sustainable operation isn't possible in arguably everything from the functionality of biological organisms [15] to the reliability of electronic [1,16], photonic [17], and electro-chemical devices [18], to high-speed transportation [19] and materials manufacturing [20]. For today's technologies, there seems to be a ubiquitous trend towards increasingly smaller, more capable, and higher energy or power density devices. Subsequently, without concurrent advances in energy efficiencies, these smaller and/or more powerful devices require improved thermal management systems to maintain their temperatures within operational limits at higher heat flux conditions.

This work revisits hot-spot cooling in microchannels, focusing on the validation of our optical pump-probe method to characterize large, gradient-driven heat and mass transport.

2.2 Microscale cooling of high heat flux devices

For high heat flux thermal management, microscale cooling with liquids has become a promising alternative to traditional air cooling due to the liquids' larger heat capacity, thermal conductivity, and intrinsic ability to dissipate large amounts of thermal energy (heat) – or regulate fluctuations in surface temperature – via liquid-vapor (latent heat) phase transformations. In result, there has been significant interest by academia and industry on convective and phase-change heat transfer at the micro- and nano-scale,

where hundreds of papers have been published on related liquid cooling processes including (but not limited to): single-phase flow [21], multi-phase flow [22,23], flow boiling [24], pool boiling [25,26], spray cooling [27,28], heat pipes [29,30], thermosyphons [31], microdroplet evaporation [32], single-phase jet impingement cooling [33,34], and micro-jet impingement boiling [35,36].

The Holy Grail for all these liquid cooling techniques is an accurate, predictive understanding of the heat transfer coefficient (h or HTC). In general, the cooling efficiency of any heat removal process is encapsulated by the HTC, which is a proportionality constant that couples the heat flux (q) to the temperature difference (ΔT) that drives the heat flow. The magnitude of the HTC is dictated by several factors, including the velocity distribution of flow-field, the thermo-fluid properties of the coolant, and surface characteristics of the device (e.g., geometry, micro-structure, temperature, and chemistry).

Table 2-1 summarizes the range in h for a variety of different cooling methods. As shown, techniques based on phase-change heat transfer (e.g., boiling and evaporation) have, most commonly, improved HTCs relative to their single-phase (e.g., non-boiling) counterparts; however, these multi-phase cooling methods also suffer from the reality that the added materials phase coincides with a much higher propensity to induce a critical or unstable “cooling regime”. In which case, the cooling performance of a multi-phase system operating in a so-called “unstable cooling regime” typically coincides with an order of magnitude reduction in the HTC. A well-known example is the onset of the critical heat flux (CHF) during nucleate pool boiling, where at CHF (and at wall superheats beyond the CHF) the HTC can decrease by several orders of magnitude [37]. Another well-known

example is the onset of wall-dryout during thin-film evaporation and nucleate flow boiling [38–40].

Table 2-1 Characteristic heat transfer coefficients (h) for different “micro-scale” cooling methods

Cooling method	**Microchannels (single-phase)**		**Microchannels (boiling)**		**Jet impingement (single-phase)**			**Jet impingement (boiling)**	
Fluid	Water	Refrigerant	Water	Refrigerant	Water	Refrigerant	Air	Water	Refrigerant
$\boldsymbol{h}$ (kW/m^2·K) [Ref]	10 – 500 [41]	1 – 30 [42]	20 – 200 [43,44]	2 – 100 [45]	30 – 320 [46]	40 – 400 [46]	5 – 400 [47]	200 – 1000 [48]	50 – 120 [46]

The optimal cooling method is also dictated by several other factors such as system size, cost of operation, and desired control scheme (i.e., active or passive). For instance, spray cooling with water is currently the most effective process for dissipating large thermal loads (i.e., heat fluxes ~10 MW/m^2) from the surfaces of moderately sized systems (e.g., surface areas < 0.5 m^2) [40,49], whereas jet impingement boiling is the optimal method for dissipating ultra-high heat fluxes (e.g., heat fluxes in the range of 0.5 – 20 MW/m^2) from sub-mm^2 sized hot-spots [35,50].

To date, the largest HTCs are observed with techniques based on jet impingement boiling. Interestingly, for sub-cooled jet impingement boiling, the HTC at the edge of the stagnation zone is found to decrease with increasing wall temperature until the onset of nucleate boiling [48], supporting that the local maximum in the HTC is at the edge of the stagnation zone and coincides with the cooling region where no phase-change and only sensible heat transfer takes place [51]. Within the stagnation zone the thickness of the thermal boundary layer (BL) is at a minimum and the acceleration of flow-field is at a

maximum. Recently, Mitsutake et al. [52] have shown that heat fluxes within 48% of the theoretical maximum can be obtained with jet impingement cooling. For reference, typically two-phase cooling methods achieve CHF values that are less than 10% of this theoretical limit (i.e., $q_{\mathrm{CHF}} < 0.1\, q_{\max}^{\mathrm{ktg}}$, where $q_{\max}^{\mathrm{ktg}}$ is the maximum evaporative heat flux predicted by the kinetic theory of gases) [53]. Another interesting finding for spray or jet impingement boiling is that the addition of non-condensable gases (NCGs) to coolant can increase the overall HTC [46,54]. This is a rather counter intuitive result because the addition of NCGs should effectively decrease the heat capacity and thermal conductivity of the coolant and thereby reduce the sensible heat contributions to the HTC.

The importance of the sensible heat contributions and NCGs to the HTC in two-phase cooling is not new. However, most studies correlate the boiling and evaporation performance to only the latent heat contributions and mixed results are reported for NCGs [55,56]. In support, are the past spray cooling studies by Kim and Kiger [] and the very recent pool boiling studies by Jaikumar and Kandilkar [54,57]. For the latter, the studies by Jaikumar and Kandikar showed that the record HTC values of $h \approx 800$ kW/m^2·K were observed with specific micro-pillar surfaces that presumably optimized the sensible cooling by minimizing nucleation and maximizing liquid convection at the base of the micro-pillars. We hypothesize that this sensible cooling effect at the base of the micro-pillars is directly correlated with the increased HTC observed within the stagnation zone for jet impingement boiling. In both cases, for example, the fluid flow-field presumably induces a suppression of the thickness of the thermal BL, ultimately increasing the HTC for a prescribed heat flux.

These results (among others) warrant the need to better decipher the relative significance between the different cooling mechanisms that dictate phase-change heat and mass transfer phenomena, especially at the micro- and nano-scale and at time-scales fast enough to render transient changes in the hydrodynamic and thermal boundary layers [58–61]. In micro-domains, multi-phase flow boiling and heat transfer is attributed to four key mechanisms: microlayer evaporation, interline evaporation, transient conduction, and micro-convection [59]. For reference, the sensible heat contributions discussed previously are effectively regulated by the rate at which the coolant can be heated (i.e., the rates of micro-scale conduction and convection within the thermal BL). To accomplish this level of thermo-physical characterization, new synchronized thermo-fluid diagnostics are needed that can combine high-fidelity temperature and flow-field measurements at spatial- and temporal-resolutions of < 5 μm and < 200 μs, respectively [60].

2.3 Time-Domain Thermo-Reflectance (TDTR)

In this section, the optical diagnostic method called Time Domain Thermoreflectance (TDTR) and the approach used in the Interfacial Transport Lab at UCF to characterize the local HTC in the thermal BL of flowing fluids will be introduced. TDTR is a well-established optical technique used by the thermal science community to characterize micro and nanoscale heat transport (e.g., most frequently the thermal conductivity and interfacial thermal conductance).

Interfacial thermal conductance is usually measured by optical pomp-probe methods such as Time-Domain Thermo-Reflectance (TDTR), 3-ω, or Picosecond

Transient Absorption methods or estimated by Acoustic or Diffusive Mismatch Models (AMM or DMM) or Molecular Dynamics Simulation (MDS). Here, TDTR technique which is setup in the Interfacial Transport Lab at UCF will be used in this study. TDTR is a technique that has acceptable resolution in all three criteria of space, time, and temperature. Table 2-2 shows typical resolutions for a range of nanoscale-relevant thermal measurement methods with highlighted values for the thermoreflectance (TDTR) method.

The TDTR technique uses two concentrically focused pump and probe laser beams to heat (with the pump) and then measure (with the probe) the temporal changes in heat transport in a sample [62–64]. The recently developed anisotropic version of TDTR will be also employed in this work, where nonconcentric beams are used to heat (pump) and measure (probe) the anisotropic thermal transport properties by spatially offsetting pump and probe beams in small increments [65,66].

Table 2-2 Typical resolutions for a range of nanoscale-relevant thermal measurement methods [67]

Method	Spatial resolution (μm)	Temperature resolution (K)	Response time (μs)
Near-field scanning optical microscopy	10^{-2}	10^{-1}	10
Transmission electron microscopy	10^{-2}	10^{-1}	10
Thermoreflectance	10^{-1}	10^{-2}	10^{-1}
Fluorescence	10^{-1}	10^{-2}	10
Scanning thermal microscopy	10^{-1}	10^{-1}	10^{2}
Optical interferometry	1	10^{-5}	10^{-3}
Raman	1	10^{-1}	10^{6}
Infrared thermography	10	10^{-1}	10
Liquid crystals	10	10^{-1}	10^{2}
Thermocouple	10^{2}	10^{-1}	10

The TDTR measurement principle is based on measuring rate of heat removal from a metal thin-film by its surroundings. For example, in this study, the cooling of a Ti thin-film (≈64 nm in thickness) by flowing water (top) and the FS substrate (bottom). In regards to the pump-probe aspect of the TDTR method, consider a focused pulse train of laser light (i.e., the pump beam) that heats the surface of the metal. Now, each fs pulse of the focused pump beam induces a local temperature jump (ΔT) in the metal over an area, $A \approx \pi w^2$. Then, after each fs heating event, the metal dissipates heat to its surroundings. Thus, the metal thin-film serves as both a heater and a thermometer, where the rate of heating is nearly instantaneous (e.g., fs heating) and the rate of cooling is dictated by the overall thermal conductance (or thermal effusivity - e_{th}) of the surroundings. For example, the cooling rate becomes more rapid by increasing either the thermal conductivity (Λ) or heat capacity (C_p) of the surroundings.

The thermometry aspect of TDTR is accomplished by the probe beam. For example, a short time-delay after each pump heating event (e.g., $\delta t = \tau_d$), the probe beam (also, a focused, pulse train of laser light) “probes” the change in temperature of the metal. The probe beam actually “probes” the change in reflectivity of the metal, which is coupled to the metal’s local temperature by its thermoreflectance coefficient (dR/dT). Hence, the name of the TDTR technique: time-domain thermoreflectance.

TDTR measured data should be compared to a heat transfer model of the sample in order to analyze the result. The model is used here has columns of heat conductivity, volumetric heat capacity, and thickness of all the material layers and interfaces between them. Unknown thermal parameters are determined by minimizing the difference between measured data and model [62].

CHAPTER 3: EXPERIMENTAL SETUP AND METHODOLOGY

This chapter is divided into three sections. In the first two sections, details about the sample stage and flow loop including microchannel fabrication, samples, and video imaging and about TDTR optical and data acquisition setup are explained. The last section discusses the method used for data reduction and uncertainty analysis.

3.1 Sample stage and flow loop

Figure 3-1 provides a schematic overview of the microchannel sample stage and flow loop of the experimental setup. It shows the flow-loop methodology based on the use of a custom syringe pump design that incorporates fluid pumping via two identical syringes (36 mm, inner diameter) with bonded plunger ends. All reported experiments are for fluid flow in the indicated flow direction; however, the flow direction can be easily reversed and reversed flow has no noticeable effect for local measurements in the center of the microchannel (data will be presented later). This is expected since the experiment is done at atmospheric pressure and flow direction is horizontal so there is no gravity effect on the flow direction and the data. The current setup facilitates volumetric flow rates ranging from 0.2 mL/min to 55 mL/min, which corresponds to ranges in average flow velocity ($\vec{\mathrm{v}}_{\mathrm{avg}}$), mass flux ($G$), and Reynolds number ($\mathrm{Re}_D$) with our microchannel setup of $0.01 \lesssim \vec{\mathrm{v}}_{\mathrm{avg}} \lesssim 3.8$ m/s, $13.9 \lesssim G \lesssim 3808$ kg/m^2/s, and $7 \lesssim \mathrm{Re}_D \lesssim 2031$, respectively. Most of reported experiments are based on a pumping rate of 50 mL/min, corresponding to $\mathrm{Re}_D \approx 1850$ using atmospheric pressure and room temperature water-inlet properties for the fluid, unless otherwise mentioned. For precise alignment, the microchannel sample

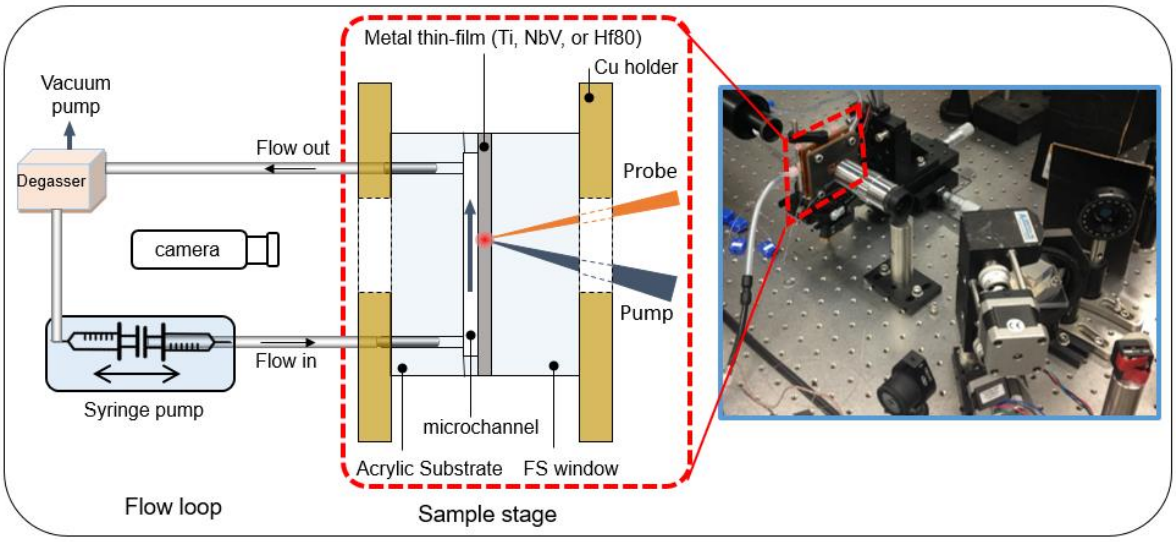

Figure 3-1 Sample stage and flow loop of the experiment.

stage is mounted on 6-axis stage, providing three (3)-translational and three (3)-rotational axes (or degrees-of-freedom) for translation and alignment.

3.1.1 Microchannel

Figure 3-2 provides an expanded view of the construction and design of the microchannel sample stage. As shown, the microchannel consists of three primary pieces: an Acrylic polymer substrate (1 inch, diameter; 1/8 inch, thick), a micro-patterned Polydimethyl-siloxane (PDMS) seal (≈ 400 μm, thick), and a metal-coated fused silica (FS) glass window (1 inch, diameter; 1/16 inch, thick). The microchannel is constructed by pressure sealing the acrylic substrate to the metal-coated FS window. The microchannel geometry (or cutout in the PDMS seal) is fabricated by laser ablation processing of the microchannel negative in an Acrylic piece and then molding the PDMS mixture in the negative by heat curing at 130 ˚C for 25 minutes. Laser ablation patterning

is also used to make the fluid inlet- and outlet-ports (≈ 1 mm, diameter) in the acrylic substrate. After pressure sealing, the microchannel dimensions are verified using the camera imaging setup shown in Figure 3-1. No leaking of the PDMS seal or flow-loop is observed for the maximum allowable flow rates of 55 mL/min. however finding the right sealing pressure in a way that there is no leaking and no flow blockage or microchannel dimension change due to the PDMS flexibility and softness is a tedious and difficult task which achieved by try and error. The microchannel length, width, and height dimensions are $L \approx 15$ mm, W ≈ 600 μm, and H ≈ 400 μm, respectively. These channel dimensions correspond to a hydraulic diameter of $D_h \approx 480$ μm by this equation:

$$D_h = \frac{2HW}{H+W} = 480\ \mu m \tag{3-1}$$

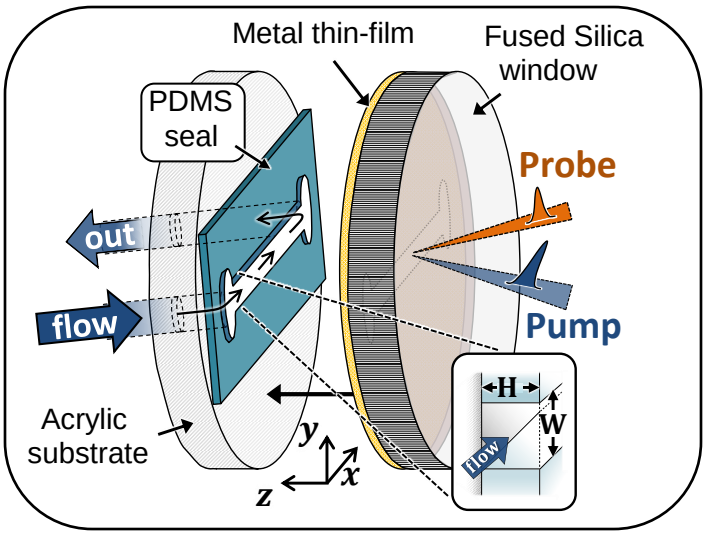

Figure 3-2 Expanded view of the microchannel construction

3.1.2 Samples

Th samples in the experiments conducted in this research work are 1 inch, diameter and 1/16 inch thick fused silica (FS) windows coated with different 50-100 nm metals or alloys. Metals or alloys with large thermoreflectance coefficients are ideal for TDTR. Aluminum (Al) is widely used in thermoreflectance experiments because of its broad applications in microelectronics, superior thermal properties, and relatively high thermoreflectance coefficient (dR/dT). However, because of the Al corrosion in contact with water and heat flow (which will be discussed later) it is not a reliable and good choice as a transducer for solid-liquid interfaces. So, other metals such as Titanium (Ti) and alloys such as NbV or Hf80 were tested and investigated.

Ti shows better stability in contact with water and has variety of applications in high heat flux cooling systems. The NbV alloy used by Feser and Cahill is also one such thin-film alternative to Al [66]. Moreover, of importance to the water flow studies in this dissertation, NbV alloys have corrosion resistance properties that are superior to Ti. In addition to Ti and NbV, a complex metal alloy consisting of Hf, Gd, and HyMu80 alloy (which we call Hf80 due to its highest Hf content) is also used. This Hf80 metal alloy not only has a low thermal conductivity (e.g., $\Lambda \cong 5.6$ W/m·K), but it is incredibly robust, facilitating later TDTR studies of flow boiling and jet-impingement with extreme hot-spot heat fluxes. All these thin-films are deposited on the FS substrates by physical vapor deposition techniques.

3.1.3 Imaging

Imaging using high speed cameras is an essential part of any micro and nanoscale flow and heat transfer studies. In the current heat transfer investigations in the microchannel using TDTR the camera setup facilitates flow visualization and alignment of the pump-probe lasers in the microchannel. Note that there are two cameras, the main one in the backside of the stage mainly used for flow visualization which we may refer as the back camera and another one in stage front for TDTR beams alignment which is referred as the front camera. The back camera is a Flea3 USB 3 camera with 150 FPS at 1280 x 1024 resolution which gives 6 ms or less (1 ms at smaller ROI sizes) time resolution. Since the TDTR laser lights have lots of shining and scattering reflections on the microchannel which makes the flow in the channel invisible, a short-pass filter is used before the back camera's sensor after TDTR alignment is done.

3.2 TDTR setup

Facilities for optical pump-probe diagnostic techniques are not available commercially as a package and are usually built in-house in labs based on applications, desired measurement parameters, and the budget. They consist of laser and optical elements on the optical table and data acquisition and electronic apparatus. Figure 3-3 shows our base in-house TDTR optical setup (a) and data acquisition and analysis (b) system, using the two-tint methodology [63] which will be discussed in the next two sections.

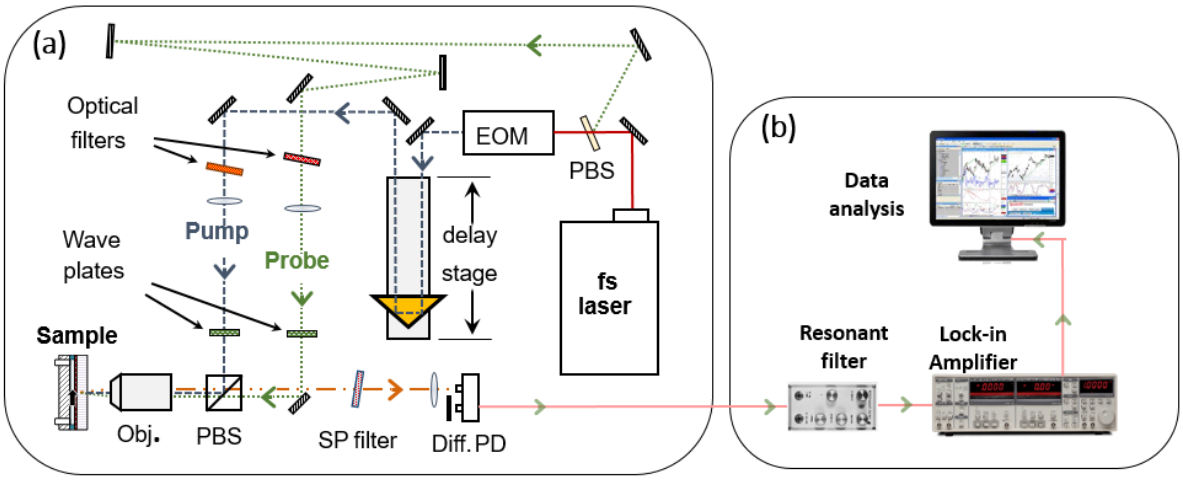

Figure 3-3 TDTR optical setup (a) and data acquisition and analysis system (b)

3.2.1 Optics

In our TDTR setup, the laser source is a Coherent Chameleon femtosecond Ti:Sapphire laser (pulse frequency: 80.1 MHz, pulse width: 140 fs, central wavelength: 787 nm). The Chameleon laser output is split into two laser beams (pump and probe). The pump beam is frequency modulated at either $f_{\mathrm{mod}} = 9.81$ MHz, 976 kHz, or 962 kHz using an Electro-Optic Modulator (EOM). The two-tint system is used to help filter (remove) pump laser light on the differential photodiode (PD) detector. After the EOM, the pump beam is reflected (down and back) using an Au retroreflector on a mechanical delay stage. After the other optics indicated in Figure 3-3 (a), the pump and probe beams are concentrically focused onto the metal thin-film on the sample using a 20× Mitutoyo, infinity corrected, long-working-distance microscope objective.

The spatial variation in the pump path length by the delay stage is equivalent to a temporal time-delay (τ_d) between each focused pump and probe pulse on the

metal/sample. TDTR setup in the Interfacial Transport Lab achieves pump-probe time-delays of -120 ps $< \tau_d <$ 3.3 ns. The focused beams waists of pump and probe beams on the metal/sample (w) are most frequently ≈9.5 μm and ≈8 μm, respectively. The incident pump and probe laser powers on the sample are adjusted to maximize the measurement signal (for a minimum amount of probe power) while also ensuring that total dc temperature rise/heating of the pump-induced hot-spot is no more than 60 K (typically, $<$ 11 mW and $<$ 5 mW for the pump and probe, respectively).

3.2.2 Data acquisition

A differential PD detector used to measure the probe's thermoreflectance signal of the sample as a function of τ_d, where again this thermoreflectance signal is induced via the frequency-modulated heating by the pump beam. The time-domain voltage output of the detector is measured by a lock-in amplifier at a reference frequency equal to f_{mod}, using triple-shielded RF coax-cables and a resonant band-pass filter between the detector and the lock-in amplifier (see Figure 3-3 (b)). The lock-in amplifier extracts the detector voltage signal into in-phase (V_{in}) and out-of-phase (V_{out}) voltage components in the frequency-domain. These voltages as a function of pump-probe delay (τ_d) are then compared to the predictions of a TDTR thermal transport model to extract the thermal properties of the sample.

We use, as most commonly done by others, the in-phase to out-of-phase voltage ratio (V_{in}/V_{out}) to correlate the time-domain changes in the surface reflectivity to the thermal transport properties of the sample [62,64,68]. In short, the TDTR voltage ratio (V_{in}/V_{out}) is the key measurement parameter for characterizing the thermal transport

properties of a sample. This work shows how measurements of V_{in}/V_{out} can be used to extract the local HTC of flowing and stagnant fluids.

3.3 Errors and uncertainty

The phase of the lock-in amplifier, modulation frequency, film thickness, the beam spot size, and the laser intensity and resulting temperature rise are common sources of uncertainties in TDTR experiment [69,70]. Uncertainties related to the phase and temperature rise are relatively small for modulation frequencies larger than 1MHz and dc heating less than 20 K. The error between the data and the model is minimized by adjusting the model parameters. Error bars associated with the standard deviation of the average values from repeated measurements at the same spot are shown in the plots.

CHAPTER 4: SINGLE PHASE HEAT TRANSPORT USING TDTR

4.1 Baseline TDTR measurements

The TDTR method does not require a calibration. Rather, the measurement accuracy is validated by reproducing thermal property data of known materials systems using no free parameters in the TDTR thermal transport model. In this regard, the TDTR method is not limited by its measurement resolution; rather, TDTR is limited by its measurement precision (i.e., reproducibility of a measurement). In principle, the technique can measure a local, transient HTC within the range of 100 kW/m^2/K $\lesssim h \lesssim$ 500 MW/m^2/K over spatial measurement areas within 10 – 2500 μm^2 and at a minimum temporal time-scale of ≈100 μs. This predicted range of TDTR measurement-space for the HTC is based on (*i*) a practical range in thermal conductivities that can be measured with the TDTR (e.g., 0.01 $\lesssim \Lambda \lesssim$ 3000 W/m/K), (*ii*) a practical range in the footprint/measurement area for the focused pump-probe lasers (e.g., 10 $\lesssim w^2 \lesssim$ 2500 μm^2), and (*iii*) the minimum time-constant setting (τ_{m}) of a MHz bandwidth lock-in amplifier (i.e., $\tau_{\mathrm{m}} = 100$ μs). We note that this discussion did not consider the length-scale that the HTC is probed within the thermal BL. This topic is addressed in section 4.2. It should also be pointed out that the precision of HTC measurements in this setup (discussed later) were observed to be within $\delta h \approx \pm$ 100 kW/m^2/K.

In order to verify the experimental setup and confirm the thermal properties of the metal thin-film heater, water, FS substrate, and other parameters in the TDTR model, full

time-delay TDTR scans have been conducted and repeated with both air and water in contact with the Al and Ti coated FS substrates.

4.1.1 Aluminum-water interface

Aluminum (Al) is widely used in thermoreflectance experiments because of its broad applications in microelectronics, superior thermal properties, and relatively high thermoreflectance coefficient. A preliminary front-side TDTR experiment was performed with the experimental details mentioned previously using ~66 nm of Al on a FS substrate using literature thermal properties [58]. The resulting data good (i.e., no free parameter) fits between the model and measured data other than the interfacial conductance (G) between the Al layer and the FS substrate ($G_{Al\text{-}FS}$ =150 MW/m^2-K) which is within the expected range measured by others and validates our experimental methodology and TDTR setup.

For Al-water interface measurements in the microchannel the results are not consistent and the ratio changes with time and from one spot to another. The reason for this inconsistency is that when Al is in contact with water is corroded uniformly or locally by water flow (flow-assisted corrosion) [71] and/or by increasing temperature of the Al or water (temperature-assisted corrosion) [72]. Such corrosion effects commonly result in pitting and deterioration of the Al surface (visible by the eye) and significant changes in the Al thickness and reflectivity.

4.1.2 Titanium-water interface

Ti-based thermal management solutions for high heat flux applications have been developed in the recent years because of its preferable mechanical, and thermal properties which includes higher strength to weight ratio, and closer thermal expansion coefficient to silicon-based chips [73]. Furthermore, it does not erode and corrode in flowing aqueous environments and shows more stability at higher temperatures in liquid cooling applications.

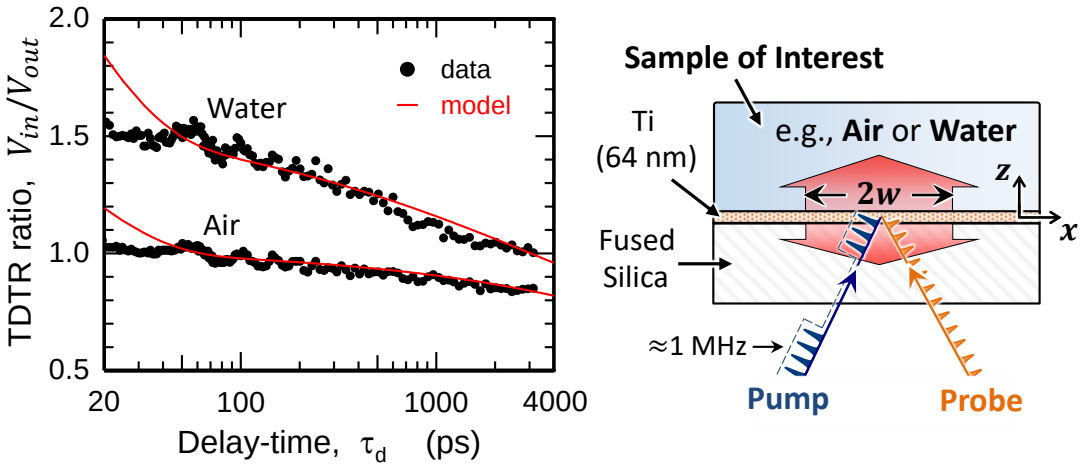

Figure 4-1 TDTR ratio data (symbols) and model predictions (lines) as a function of pump-probe delay-time for a Ti-coated FS glass window in thermal contact with non-flowing (stagnant) water or air in the microchannel (f_{mod} = 962 kHz).

After validation of the experimental setup with Al sample, a ~64 nm Ti layer on a 1" FS substrate is selected as the base sample for the rest of the experiments. Figure 4-1 shows the predicted V_{in}/V_{out} ratio as a function of pump-probe delay (τ_d) with comparisons to measured data for both air and non-flowing (stagnant) water in contact with a Ti metal coated FS glass window. The model predictions (lines) are based on literature thermal property data for the fluid (air or water), Ti thin-film, and FS glass

substrate. The TDTR experiments and modeling with an air-filled microchannel are used to determine and validate the thermal properties of Ti and FS (which are also used and verified repeatedly for all subsequent TDTR experiments). For example, the measured thermal conductivity and volumetric heat capacity of Ti were $\Lambda^{Ti} = 20\ W/m.K$ and $C_p^{Ti} = 2.384 \times 10^6\ J/m^3.K$, respectively, which are in good agreement with literature data for Ti.

The schematic in Figure 4-1 corresponds to the materials and measurement configuration, where the pump-probe beams pass through the FS glass substrate and then heat the "backside" of the Ti thin-film. The data in Figure 5 shows that the magnitude of V_{in}/V_{out} is larger for the more thermally conductive fluid – i.e. water (as opposed to air) in the microchannel. Also, for these "backside" TDTR measurements, oscillations in V_{in}/V_{out} are observed (see, Figure 4-1) – presumably due to Brillouin backscattering in the glass substrate [64]. We point out the oscillation peak at 100 ps because this study uses V_{in}/V_{out} measured at a single delay time (i.e., $\tau_d \approx 100$ ps) to predict the HTC of flowing fluids. Thus, our measured fluid thermal conductivities and corresponding HTC predictions will be slightly overestimated (e.g., 5-20 %, with and without fluid flow) based on V_{in}/V_{out} measured at solely $\tau_d \approx 100$ ps. Conversely, underestimates are found using V_{in}/V_{out} measured at solely $\tau_d \approx 80$ ps because an oscillation valley exists at that delay time.

As illustrated in Figure 4-1 (schematic), the heat load from the hot-spot (laser) is transferred into both the fluid and the FS glass substrate. If the fluid is air, then nearly all the heat goes into the substrate (e.g., $e_{th}^{\mathrm{air}} \ll e_{th}^{\mathrm{FS}}$). Whereas, if the fluid is water, then heat load is nearly split equally between FS substrate and the water coolant (e.g., $e_{th}^{\mathrm{water}} \approx e_{th}^{\mathrm{FS}}$). We note that the HTC measurement sensitivity can be improved by replacing the FS

substrate with a different optically transparent, thermally resilient substrate having an ultra-low thermal conductivity (or eliminating the substrate altogether). Due to the lack of a practical alternative to FS glass, all studies are conducted with microchannels on metal-coated FS glass.

4.2 Heat transfer in thermal BL in microchannels

Heat transport between a channel and the fluid flowing inside it occurs at the fluid-channel wall interface in the vicinity of thermal boundary layer [74]. Knowledge of flow-field development, channel dimensions, and their effect on BL formation, growth, and thickness are required for identifying the best and applicable method (in terms of time- and length-scales) for characterization of BL heat and mass transport

4.2.1 BL growth in microchannels

It has been verified that the flow regimes inside microchannels are typically described by developing hydrodynamic and thermal BLs with laminar flow [75]. It has also been suggested that the flows in microchannels can be considered as fully-developed (hydrodynamically) because of the typical sudden contraction at the inlet [76]. As it's calculated by the equation (3-1) in section 3.1.1 Hydraulic diameter of a rectangular channel is $D_h = 480\ \mu m$, which is ~1/2 the diameter of the water entrance- and exit-ports and, thus, we can assume the flow hydrodynamically fully developed. For microchannels with $D_h > 1\mu m$, most of the liquids (including water) can be treated as continuous media with the same classical rules and correlations for macro-channels [77].

For microchannels with $D_h < 1mm$ and laminar developing flow BLs from the channel walls, the hydrodynamic BLs converge and induce BL mixing (as shown in Figure 4-2). To describe thickness of the thermal and hydrodynamic BLs, we use the expressions $\delta = 5x/(Re_x)^{0.5}$ and $\delta_t = \delta/(Pr)^{1/3}$, respectively [78]. For example, in the current work with $D_h = 480\ \mu m$ and a flow rate of $Q = 7.66\times10^{-4}\ L/s\ = 46\ mL/min$ which corresponds to $Re \approx 1750$, both hydrodynamic BLs coverage/overlap at a distance of $2 < x_e < 3\ mm$ from the fluid-inlet. This length (x_e) is known as "entry length" which is different than entrance length for the fully-developed condition. Thus, the hydrodynamic BL thickness would be more than the channel height after the middle of the channel for $D_h = 480\ \mu m$ and $Re \approx 1750$. However, in developing areas, BL thickness is less than in fully-developed areas. Thus, in this work, hydrodynamic BL convergence in microchannel pushes the BL toward the channel walls and make it thinner than predicted using $\delta = 5x/(Re_x)^{0.5}$.

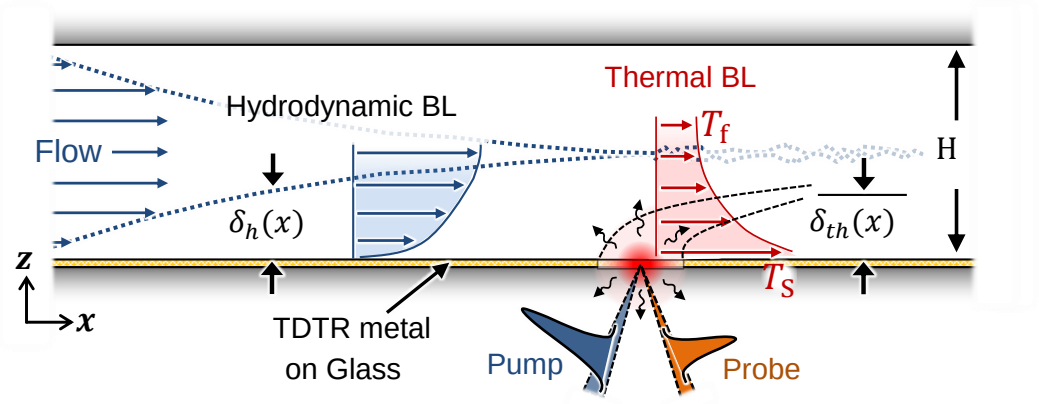

Figure 4-2 Schematic illustrations of both Hydrodynamic BL growth ($\delta_h(x)$) in a microchannel of height (H ≈ 400 μm) and Thermal BL growth ($\delta_{th}(x)$) from a hot-spot in the metal-coated glass wall by the TDTR pump-probe lasers

Heat loads in microchannels and electronic cooling applications are rarely spatially and temporally uniform, where partial, periodic, or spot heating are most commonly realized [79]. If heating starts at a relatively large distance from the channel inlet (or there is a partial or periodic heating), then the thickness of the thermal BL (δ_t) is much less than δ. Figure 4-2 shows a thermal BL (with exaggerated thickness) developed after the channel wall is heated by a laser. Using $x = w_0$ (or $x = 2w_0$), the thermal BL thickness corresponds to $\delta_t = 0.7\ \mu m$ (or $1.4\ \mu m$), respectively. Then, as depicted in Figure 4-2, δ_t rapidly decays after a short distance from the laser heating spot.

4.2.2 TDTR in thermal BL region

TDTR is very well known for its capability in nondestructively and accurately sensing the temperature change and the resulting heat transport at the micro- and nano-scales. In this method, the probe beam measures the temperature oscillations within the Thermal Penetration Depth (ℓ_{th}) of the experiment in heat flow direction. This depth can be estimated as $\ell_{th} = (D_t/\omega)^{1/2}$, where D_t is the thermal diffusivity of the medium and ω is the angular heating/modulation frequency ($\omega = 2\pi f$). Our experiments with water ($D_t = 1.47\times10^{-7}\ m^2/s$) and the used heating frequencies of $f = 9.81\ MHz$ and $f = 962\ KHz$ correspond to thermal penetration depths of $\sim 225\ nm$ and $\sim 70\ nm$, respectively.

Figure 4-3 provides the predicted thicknesses of thermal and hydrodynamic BLs as a function of Re number. For comparison, Figure 4-3 also provides the predicted thermal penetration depths for water as a function of modulation frequency. As shown in Figure 4-3, the thermal penetration depth of a TDTR experiment and the thermal BL thickness are only comparable in magnitude at low modulation frequencies and high Re

numbers. In the cross-hatched region of the Figure 4-3 (lower right corner), the thermal penetration depth is larger than the thickness of the thermal BL ($\ell_{th} > \delta_t$), which is ideal for detailed and accurate TDTR characterization of the thermal transport inside the boundary layer and corresponding flow-field effects. Nevertheless, small thermal penetration depths, such as $\sim 390\, nm$, are thick enough to capture and record temperature oscillations near the liquid-wall interface using the TDTR measurement technique.

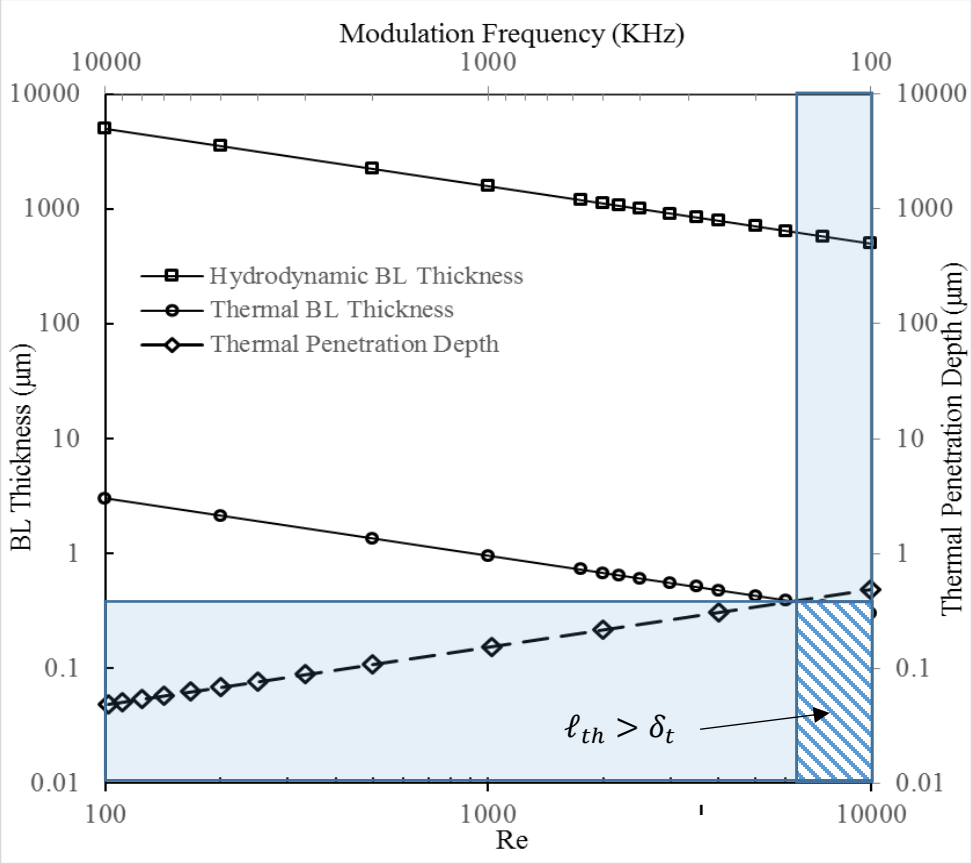

Figure 4-3 Hydrodynamic and thermal BLs thicknesses verses Re number (left-bottom axes, respectively). Thermal penetration depth verses modulation frequency (right-top axes, respectively).

4.2.3 Anisotropic TDTR measurements

In the previous sections, we described the setup and measurement principle for the traditional TDTR method. The traditional TDTR method (based on two concentrically focused pump and probe beams) is most commonly used to measure the through- (or cross-) plane thermal conductivity ($\Lambda_{\perp}$) of the sample (i.e., Λ in the perpendicular ($\perp$) direction from the metal thin-film). The TDTR method and modified versions can also be used to measure the in-plane thermal conductivity ($\Lambda_{\parallel}$), which is of interest for studies of materials with thermal transport anisotropy [80,81]. Furthermore, it has been shown both numerically and experimentally that if the in-plane thermal diffusion length is comparable to the beam size then the TDTR measurement signal is more sensitive to the in-plane thermal transport [65,82]. Recent work by Feser et al. [65,66] have proposed the approach of using spatially offset (or non-concentrically focused) pump and probe beams to measure both $\Lambda_{\perp}$ and $\Lambda_{\parallel}$. In their method (which called “Anisotropic TDTR”) the pump beam heats the metal thin-film and then the probe beam senses the rate of surface temperature change (decay) at different lateral locations.

Figure 4-4 illustrates the anisotropic TDTR method with additional illustrations related to the thermal and hydrodynamic BLs of fluid flow-field. As shown in Figure 4-4, by spatially offsetting the pump and probe beams, the anisotropic TDTR method can probe heat transport inside and outside the “pump-induced” thermal BL. In my experiments, the probe beam is actually at a fixed location in the microchannel and I displace the pump beam up- and down-stream of the probe. However, for simpler illustration and descriptions later we show the opposite to help emphasize our probing of

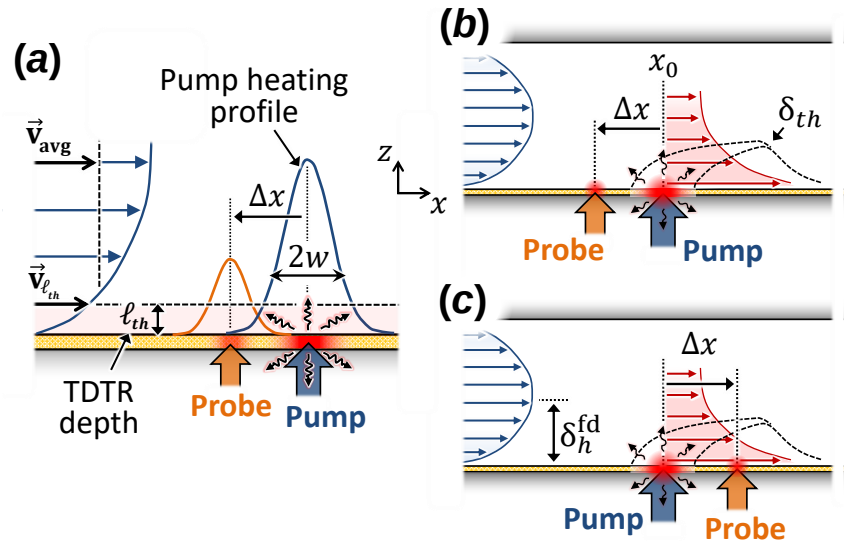

Figure 4-4 Schematic illustration of the anisotropic TDTR method with a flowing fluid (not-to-scale), where Δx is the pump-probe offset, w is the pump beam waist, $\vec{v}_{avg}$ is the average flow field velocity, and l_t is the thermal penetration depth. (b) and (c) Probing up-stream and down-stream (or within) the pump-induced thermal BL, respectively.

heat transport up-stream and down-stream the "pump-induced" thermal BL (see, Figure 4-4 (b) and (c), respectively). For reference, these displacements are small and are typically at most twice the pump's focused beam waist (i.e., $|\Delta x| \leq 2w$, where $w \approx 9.5$ μm). In this setup, pump beam displacements relative to the probe can be produced along both the x- and y-axis directions. Displacements of the pump beam are accomplished by rotating the polarized beam splitter (PBS) shown in Figure 3-3 with a custom two-axis (stepper-motor controlled) galvo-stage. The galvo-stage has a displacement resolution along the x-axis (i.e., flow-field axis) of ≈0.0935 μm/μ-step. For reference, 25 μ-steps of the x-axis stepper motor corresponds to a ¼ w offset of the pump relative to the probe.

4.2.4 Effect of flow field

For both the traditional and anisotropic TDTR methods, the heat transport measurements are described to take place within a region of thickness ℓ_{th} from the metal thin-film. This thickness (or depth) in a TDTR measurement is also illustrated in Figure 4-4 (*a*) with respect to the flow-field velocity. For reference, $\ell_{th} \approx 225$ nm for room temperature TDTR studies with water on Ti-coated glass and $f_{\mathrm{mod}} \approx 962$ kHz, where increasing the modulation frequency to $f_{\mathrm{mod}} \approx 9.81$ MHz corresponds to $\ell_{th} \approx 70$ nm. In either case, this is a very thin region and the maximum flow field velocity we can obtain within this short distance (ℓ_{th}) from the metal surface is $\vec{\mathrm{v}}_{\ell_{th}} \approx 0.016$ m/s (based on a Hagen-Poiseuille flow-field). However, the flow-field outside ℓ_{th} still influences the heat transfer within ℓ_{th}. Nevertheless, this estimate for $\vec{\mathrm{v}}_{\ell_{th}}$ is based on the microchannel testing conditions/geometry and a fully-developed flow profile with no-slip at the metal/fluid interface. For reference, the maximum flow velocity in the center of the channel is $\vec{\mathrm{v}}_{\mathrm{max}} \approx 6.94$ m/s (i.e., the flow 200 μm from the metal/glass wall, using $\vec{\mathrm{v}}_{\mathrm{max}} = 2\,\vec{\mathrm{v}}_{\mathrm{avg}}$ and a volumetric flow rate of 50 mL/min from the syringe pump).

For comparative purposes, we compare this flow-field velocity in the TDTR measurement region (i.e., $\vec{\mathrm{v}}_{\ell_{th}}$) to the velocity that thermal energy propagates by heat conduction in the fluid (e.g., the group velocity - $\vec{\mathrm{v}}_g$). Considering the common real-part of the group velocity, thermal energy within ℓ_{th} propagates at $\vec{\mathrm{v}}_g = 4\sqrt{\pi f_{\mathrm{mod}} D_{th}}$ [83], which for our experiments with near room temperature water and $f_{\mathrm{mod}} = 962$ kHz corresponds to $\vec{\mathrm{v}}_g \approx 2.7$ m/s. This group velocity for thermal energy transport is a factor of 100 greater than $\vec{\mathrm{v}}_{\ell_{th}}$; yet, $\vec{\mathrm{v}}_g$ is still 61% and 21% less than $\vec{\mathrm{v}}_{\mathrm{max}}$ and $\vec{\mathrm{v}}_{\mathrm{avg}}$, respectively. The latter is

pointed out because if we consider ℓ_{th} as the TDTR measurement region, then a flowing fluid outside ℓ_{th} (i.e., the "fluid surroundings" outside the ℓ_{th} boundary is comprised of higher velocity and lower temperature water) would still be influencing the heat and mass transport within ℓ_{th}. However, for a stagnant fluid, $\vec{v}_g \gg \vec{v}_{\max}$, and thus, only conductive heat transport is dominant – which will be discussed in the next section 4.3.

Increasing the flow rate (or Re number) for a given channel dimensions makes the BL thickness thinner and increases the amount of flow, turbulence and mixing inside BLs which all augment the rate and amount of the heat transport and finally enhance overall heat transfer [84,85]. The Nusselt number (Nu) is another important dimensionless parameter commonly used in convective heat transfer studies, where Nu is defined as the ratio of convective to conductive heat transfer at boundaries between wall and fluid. The $\boldsymbol{Nu}$ number is related to the HTC by:

$$Nu = HTC.\, l/\Lambda \tag{4-1}$$

where l is a characteristic length and Λ is thermal conductivity of the fluid. The effect of Re number on Nu number in rectangular microchannels with widths ranging from 194 μm to 534 μm at $Re = 300 - 3500$ has been extensively studied by Lee et al. [75]. They found a good agreement between their results for microchannels and literature data for conventional channels using classic analysis, concluding that the Nu number increases similarly with Re number in microchannels. Another study by Mansoor et al. recently investigated heat transfer in the simultaneously (both hydrodynamically and thermally) developing region of a microchannel with $D_h = 318\ \mu m$ with base heat fluxes ranging from

45 to 130 W/cm^2 [86]. The simulations confirmed previous experimental results, yielding the correlation for average Nu number:

$$Nu = 0.2931 Re^{0.53} Pr^{-0.25} \qquad 500 \leq Re \leq 2000 \tag{4-2}$$

where Pr is Prandtl number.

Size of the typical measurement devices (e.g. temperature or pressure sensors tips) are comparable to microchannels dimension and there are space, access, and resolution limits in local parameters measurements in microfluidics. Most of the experimental studies in this area focused on an average Nu number for a microchannel (or total heat transfer coefficient for a set of microchannels). Using TDTR, we quantify thermal transport locally at different flow rates. For this purpose, the ratio in TDTR experiment was measured at $x/l = 0.5$, using delay-times of $\tau_d = 100\ ps$ and $500\ ps$ and flow rates $0 - 50\ mL/min$ in the microchannel. This ratio was then used to extract effective heat conductivity (Λ_{eff}) from the model using previously established model parameters.

Figure 4-5 shows the measured TDTR ratio at different delay-times as a function of water flow rate. Based on this plots the ratio starts to increase with the flow rate quickly when still water starts to flow inside the microchannel for both delay-times. Then it increases with the flow rate gradually until it remains nearly constant beyond a specific flow rate which is $40\ mL/min$ for this channel size and the heat flux. Plots of two correlations for average Nusselt number ($\overline{Nu}$) of simultaneously developing internal laminar flow with constant wall heat flux have been also added to the Figure 4-5 for comparison from the literature. The first one (Equation 4-2) is for a rectangular micro-

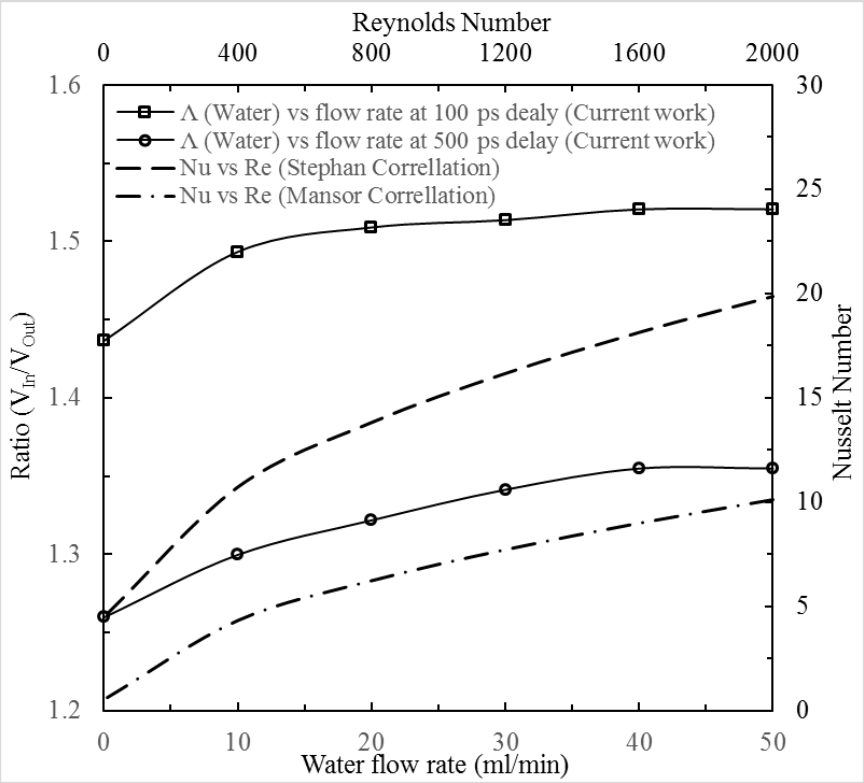

Figure 4-5 Comparison between the measured TDTR ratio at different flow rates and delay times and the $\overline{Nu}$ correlations in the literature. Dashed and dash-dot are for simultaneously developing flow with constant wall heat flux using equation (4-3) in a circular duct [87] and equation (4-2) in a rectangular microchannel [86].

channel [86] and the second one is for a circular duct with the correlation of [87]:

$$Nu = 4.364 + \frac{0.086(RePrD_h/L)^{1.33}}{1+0.1(RePrD_h/L)^{0.83}} \tag{4-3}$$

Both correlations present similar trends, however Stephan's correlation predicts $10 < Nu < 20$ which is in the range reported for microchannels with $500 < Re < 2000$ [75]. Furthermore, equation (4-3) is more realistic for lower Re numbers. When there is no flow ($Re = 0$) the equation gives $Nu = 4.363$, which can be interpreted as the thermal diffusion and natural convection contributions to the heat transport [88]. It should be noted

that the fit parameter Λ_{water} in TDTR model also includes all heat transfer mechanisms present in the experiment [58]. From the similar trends between the TDTR data and the Nu correlations it's supposable that there should be a relation between TDTR data and HTC or Nu.

4.3 HTC predictions via TDTR

The dependence of V_{in}/V_{out} on changes in the thermal effusivity of the fluid/sample is an essential attribute of the TDTR method for characterizing the HTC of stagnant, flowing, or evaporating fluids. The following is the derivation of the HTC in terms of the fluid's thermal effusivity. It starts with the standard expression for the HTC:

$$h = q/\Delta T \tag{4-4}$$

where, for the TDTR method, the heat flux into the fluid is

$$q = \tilde{P}_{laser}/\pi w^2 \tag{4-5}$$

and the temperature difference between the metal surface and the fluid outside the thermal BL (due to AC pump heating at $\omega = 2\pi f_{\mathrm{mod}}$) is

$$\Delta T_{AC} = [\tilde{P}_{laser}/\pi w^2][1/e_{th}\sqrt{\omega}] \tag{4-6}$$

Equation (4-6) is based on the solution by Carslaw and Jaeger for periodic surface heating in a semi-infinite solid [89,90]. It is still valid for stagnant fluids, where here $\tilde{P}_{\mathrm{laser}}$ represents the average laser power of the modulated pump beam at ω that is absorbed by the metal thin-film and is transported as heat into the fluid over the heating area (πw^2).

Inserting equations (4-5) and (4-6) into equation (4-4), this heating power per unit area cancels out and we have the following HTC equation for the TDTR method:

$$h = e_{th}\sqrt{\omega} = \sqrt{2\pi f_{\mathrm{mod}}\Lambda \mathrm{C}_p} \approx \frac{\mathcal{C}}{\sqrt{t_c}} e_{th} \tag{4-7}$$

The right-hand term in equation (4-7) is included to emphasize that the HTC is proportional to the thermal effusivity of the fluid. In particular, e_{th} within the TDTR measurement region (i.e., e_{th} within the thermal BL of the pump induced hot-spot). In equation (4-7), $\mathcal{C}$ is a constant, f_{mod} is the modulation frequency of pump beam and t_c is a critical (or fundamental) time-scale in a TDTR experiment for the metal thin-film to exchange thermal energy with its surroundings.

Alternatively, equation (4-7) could be derived by setting $\mathcal{C} = 1$ and relating t_c to the thermal diffusivity of the fluid/surroundings, $t_c = [\ell_{th}/\sqrt{2}]^2/D_{th}$, where

$$\ell_{th} = \sqrt{2D_{th}/\omega} = \sqrt{D_{th}/\pi f_{\mathrm{mod}}} \tag{4-8}$$

is the thermal penetration depth mentioned earlier in this chapter. It's a fundamental length-scale in TDTR [90] that corresponds to the average depth of thermal energy exchange between the fluid/surroundings and an interface that is periodically heated at ω.

In this dissertation equation (4-7) and the measured TDTR ratio data is used to extract the HTC. In short, V_{in}/V_{out} is measured at different delay times and different flow-field conditions. Then, thermal effusivity of the fluid is used as a fitting parameter to relate the TDTR model predictions to V_{in}/V_{out} data.

Figure 4-6 shows the predicted dependence of V_{in}/V_{out} on both (a) the thermal effusivity (e_{th}) and (*b*) the thermal diffusivity (D_{th}) of the surroundings. In particular, V_{in}/V_{out} for a variety of different top-layer materials (e.g., solid, liquid, or gas) for the measurement schematic shown in Figure 4-1. This data is provided to emphasize that both (*i*) the magnitude of V_{in}/V_{out} at a given pump-probe delay (τ_d) and (*ii*) the cooling rate of the Ti metal (e.g., $\Delta(V_{in}/V_{out})/\Delta\tau_d$) is mainly dictated by the thermal effusivity of the surroundings – e.g., $e_{th}^{\text{fluid}} = [\Lambda_{\text{fluid}} \text{C}_p^{\text{fluid}}]^{1/2}$. For these predictions, the thermal properties of the FS substrate ($\Lambda_{\text{FS}} = 1.32$ W/m·K, $\text{C}_p^{\text{FS}} = 1.64$ J/cm^3·K), Ti thin-film ($\Lambda_{\text{Ti}} =$ 20 W/m·K, $\text{C}_p^{\text{Ti}} = 2.38$ J/cm^3·K), and volumetric heat capacity of the sample/fluid are held constant, while Λ_{fluid} is varied to represent the range in e_{th} (or D_{th}) of different sample/fluid systems. A constant heat capacity of either $\text{C}_p^{\text{fluid}} = 4.15$ J/cm^3·K [blue-lines] or $\text{C}_p^{\text{fluid}} = 1.2$ J/cm^3·K [black-lines] is used because they represent upper- and lower-limits of C_p for various solids and liquids at room temperature.

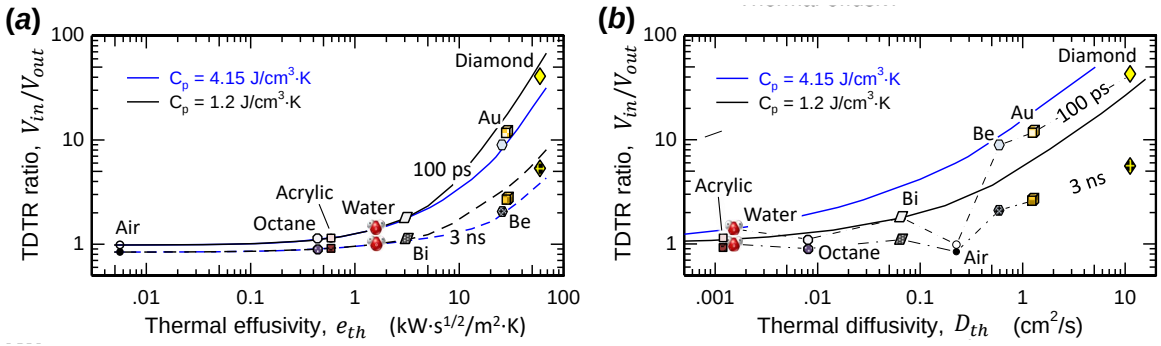

Figure 4-6 Predicted dependence of the TDTR ratio on (a) the thermal effusivity and (b) thermal diffusivity of the sample/fluid in thermal contact with a Ti-coated FS substrate . Predictions are provided for different materials (symbols) at delay times of $\tau_d = 100\,ps$ and $3\,ns$. The magnitude of the difference between the open (100 ps) and closed (3 ns) symbol data is indicative of the cooling rate of the Ti metal thin-film.

In Figure 4-6, predictions are provided for two different pump-probe delay times ($\tau_d = 100\ ps$ [solid-lines] and of $\tau_d = 3\ ns$ [dashed-lines]). I point out that for low thermal effusivity samples/fluids – e.g., $e_{th}^{\text{air}} < 0.01\ \text{kW} \cdot s^{1/2}/m^2.\text{K}$ in Figure 4-6 (*a*) – the TDTR ratio converges to that of the Ti-coated FS substrate in vacuum. Moreover, for low thermal effusivity samples the cooling rate is relatively small, where cooling rate of the metal is directly correlated with the decay rate in the TDTR ratio (i.e., $d(\Delta T)/dt \propto \Delta(V_{in}/V_{out})/\Delta\tau_d$). However, for ultra-high thermal effusivity samples (e.g., diamond) this decay rate or difference between V_{in}/V_{out} at $\tau_d = 100\ ps$ (open-diamond) and V_{in}/V_{out} at $\tau_d = 3\ ns$ (filled-diamond) is the maximum predicted. We also note that the magnitude of this difference is systematic with increases in e_{th}, whereas (as illustrated in Figure 4-6 (*b*)) the cooling rate of the Ti metal thin-film is not systematic with increases in the thermal diffusivity of the sample. In summary, the TDTR model predicts that both V_{in}/V_{out} and $\Delta(V_{in}/V_{out})/\Delta\tau_d$ are directly proportional to the thermal effusivity of the fluid; therefore, so should the HTC (as indicated by equation (4-7)), especially for heat transport in single-phase fluids.

4.4 Differential measurements of the HTC using anisotropic TDTR

While, the anisotropic TDTR method was originally proposed to measure the anisotropic thermal properties of solid thin films and bulk solids, the method can also be used to characterize homogeneous materials (e.g., isotropic fluids) and “effectively” anisotropic fluids (such as flowing water, where heat transport is influenced by direction of the flow-field). In this regard, anisotropic heat transport due to a flowing fluid is analogous to anisotropic heat transport in a solid (e.g., graphite), where, for a flowing

fluid, the moving fluid molecules (of an isotropic fluid) will induce unique changes in the measured TDTR ratio (V_{in}/V_{out}) as a function of pump beam displacement/offset.

Figure 4-7 shows anisotropic TDTR scans of the Ti-coated FS substrate with both stagnant air (filled-circles) and stagnant water (open-circles) in the microchannel. This data serves as a baseline for local HTC measurements using the differential TDTR measurement methodology, where these anisotropic TDTR scans with both stagnant air and stagnant water are needed for later HTC analysis with flowing water. We note that translating the overall pump-probe measurement ROI to a location outside the microchannel (i.e., onto the PDMS seal using the 6-axis sample stage) showed increases in V_{in}/V_{out} indicative of a polymer in contact with the Ti metal. For the experiments in Figure 4-7, the pump-probe delay and modulation frequency were fixed at $\tau_d = 100\ \mathrm{ps}$ and $f_{\mathrm{mod}} = 962\ \mathrm{kHz}$, respectively. Measurements at longer delay times (e.g., $\tau_d > 500\ \mathrm{ps}$) had more measurement noise and experiments with decreased modulation frequencies (e.g., $f_{\mathrm{mod}} < 900\ \mathrm{kHz}$) did not correlate well with the TDTR model predictions.

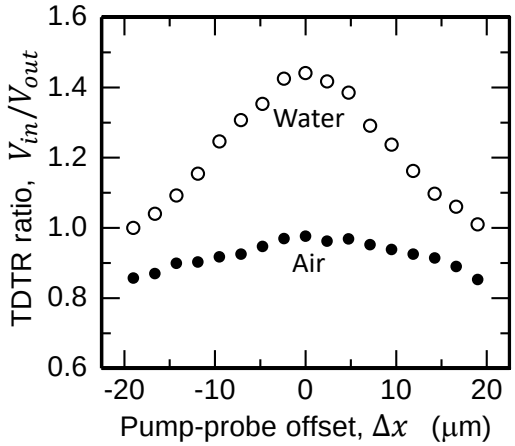

Figure 4-7 Anisotropic TDTR measurements corresponding with heat conduction and natural convection of water and air in the microchannel ($\tau_d = 100\ \mathrm{ps},\ f_{\mathrm{mod}} = 962\ \mathrm{kHz}$).

Figure 4-8 shows anisotropic TDTR scans at $\tau_d = 100\ ps$ with both stagnant water (circle-symbols) and flowing water (star-symbols) in the microchannel. Figure 4-8 (b) shows V_{in}/V_{out} measured at different pump-probe offsets (Δx) relative to the pump heating waist (w). Experiments without fluid flow are referred as "stagnant water"; however, there still may be considerable micro-convection in the vicinity of the micron-sized hot-spot induced by the pump beam, where fluid flow in the channel will magnify this micro-convection in the probe measurement ROI. Figure 4-8 (c) shows the corresponding measurements/predictions of the fluid thermal effusivity and HTC at different pump-probe offsets. As shown, water flow in the microchannel increases the effective thermal effusivity of the fluid (relative to that of the stagnant fluid).

The V_{in}/V_{out} ratio data shown in Figure 4-8 (b) was measured after acquiring the air data (filled-circles) in Figure 4-7. For example, after the air experiments, the microchannel was filled with water. Then, for a given pump-probe offset (Δx), starting with concentrically focused beams ($\Delta x = 0$ μm), the in-phase (V_{in}) and out-of-phase (V_{out}) TDTR signals for stagnant water (Re_D = 0) and then flowing water (Re_D = 1850) were repeatedly measured, including several of these dual-scan measurements at offsets ranging within -20 μm $< \Delta x <$ 20 μm (or $2w \lesssim \Delta x \lesssim 2w$). Then, the TDTR ratio (i.e., V_{in}/V_{out} in Figure 4-8 (b)) was computed for the subsequent predictions of the HTC (i.e., the data in Figure 4-8 (c)).

Currently, we do not have a validated bidirectional TDTR model for the anisotropic method, where bidirectional refers to heat transport (from the metal) into both the fluid and glass substrate. However, we do have a bidirectional TDTR model for through-plane

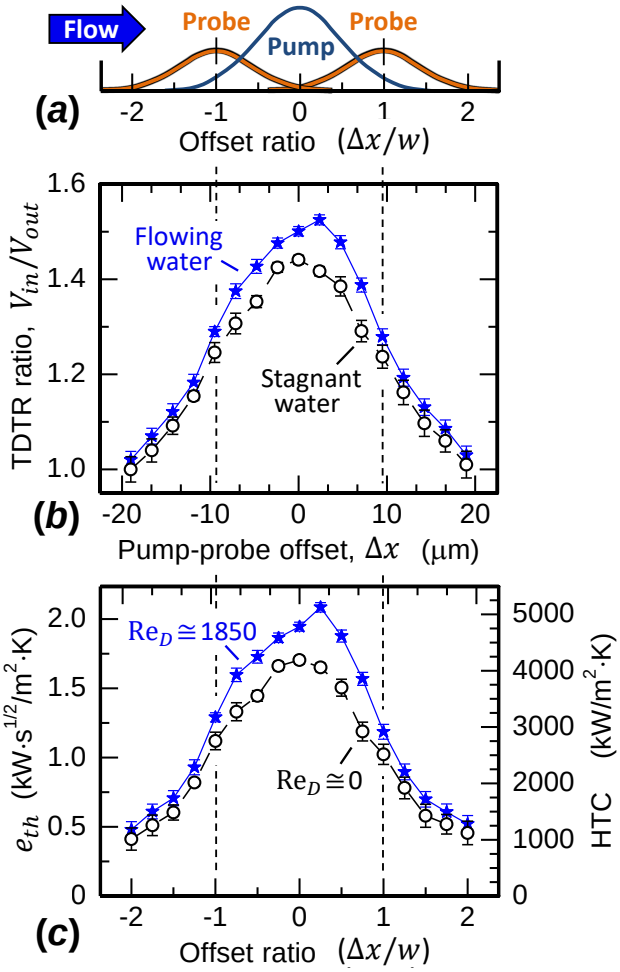

Figure 4-8 (*a*) Schematic depiction of probing up-stream ($\Delta x/w < 0$) or down-stream ($\Delta x/w > 0$) the pump induced hot-spot in the microchannel. (*b*) Anisotropic TDTR measurements for Ti-coated glass with flowing or stagnant water in the microchannel. (*c*) Corresponding thermal effusivity of water (left axis) and HTC (right axis) based on differential TDTR analysis scheme.

thermal transport based on concentrically focused pump and probe beams (see, Figure 4-1). Therefore, for HTC analysis I have employed a differential measurement/analysis scheme. This differential scheme consists of using this traditional bidirectional TDTR model to fit an effective through-plane thermal effusivity (e_{th}^{eff}) to V_{in}/V_{out} measured at

different pump-probe offsets. The data in Figure 4-8 (c) are the results of this fitting process for e_{th}^{eff} (left-axis) and the corresponding HTC (right-axis – via equation (4-7)).

We note that before we could quantify e_{th}^{eff} (or the HTC) of stagnant or flowing water, we needed to know the effective thermal effusivity of the FS substrate as a function of pump-probe offset (i.e., $e_{th}^{\text{eff}}(\Delta x)|_{\text{FS}}$). I obtain $e_{th}^{\text{eff}}(\Delta x)|_{\text{FS}}$ via TDTR model fits of the measured ratio data for air/Ti/FS in Figure 4-7, where the properties of the air, Ti thin-film, and heat capacity of FS substrate are held constant, such that $\Lambda_{\perp}^{\text{FS}}$ is the only TDTR model fitting parameter. This approach produces values for $\Lambda_{\perp}^{\text{FS}}$ at each pump-probe offset (or equivalently $e_{th}^{\text{eff}}(\Delta x)|_{\text{FS}}$ because heat capacity was held constant in this analysis). Alternatively, we have also obtained $e_{th}^{\text{eff}}(\Delta x)|_{\text{FS}}$ by fitting C_p^{FS} while keeping the other model parameters fixed at literature values. Both approaches yield the same $e_{th}^{\text{eff}}(\Delta x)|_{\text{FS}}$ results. This same fitting procedure is used to predict e_{th}^{eff} of stagnant water and flowing water as a function of Δx (i.e., the data in Figure 4-8 (c)). However, in this case, the anisotropic thermal effusivity data for the FS substrate ($e_{th}^{\text{eff}}(\Delta x)|_{\text{FS}}$) is now a known input to the TDTR model at each respective Δx offset – hence, this is the differential aspect of our anisotropic TDTR measurement methodology.

Figure 4-9 shows the measured TDTR ratio and corresponding HTC results (via differential measurement methodology) for concentric pump-probe alignment ($\Delta x/w \cong 0$) as a function of the fluid flow rate in microchannel. The data is provided for two different pump-probe delay times (e.g., $\tau_d = 100\,ps$ and $\tau_d = 500\,ps$). As expected, measurements at both delay times yield the same trends in HTC results. This data is provided to emphasize that the measured HTC enhancement due to forced convection

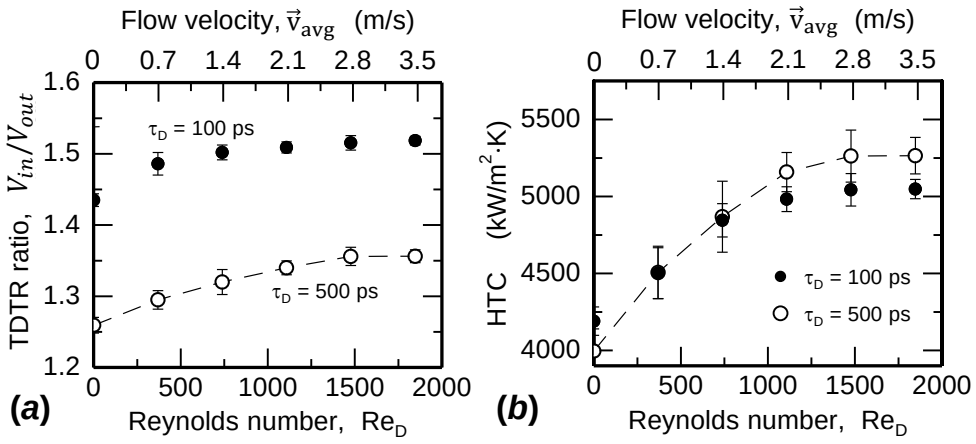

Figure 4-9 (a) TDTR ratio data and (b) corresponding HTC data at zero pump-probe offset ($\Delta x/w \cong 0$) as a function of the water flow rate in the microchannel (Ti heater/thermometer, $f_{\mathrm{mod}} = 962\ KHz$ 962, $w = 9.5\ \mu m$).

over the pump-induced hot-spot is systematic with the magnitude of the water flow rate in the microchannel.

4.4.1 Different metal thin-film case studies

To demonstrate the applicability and meaningfulness of our HTC measurements using the anisotropic TDTR methodology, several studies conducted with different metal thin-film materials deposited on FS glass substrates. As discussed in Ref. [66], the anisotropic TDTR method is more sensitive to the in-plane thermal transport (e.g., $\Lambda_{\parallel}$) using highly focused pump-probe beams and low thermal conductivity metal thin-films. In this regard, metal alloys with large thermoreflectance coefficients are ideal. The NbV alloy used by Feser and Cahill is one such thin-film alternative to Al [66]. Moreover, of particular importance to the current water flow studies, NbV alloys have corrosion resistance properties that are superior to Ti. In addition to Ti and NbV, I also used a complex metal

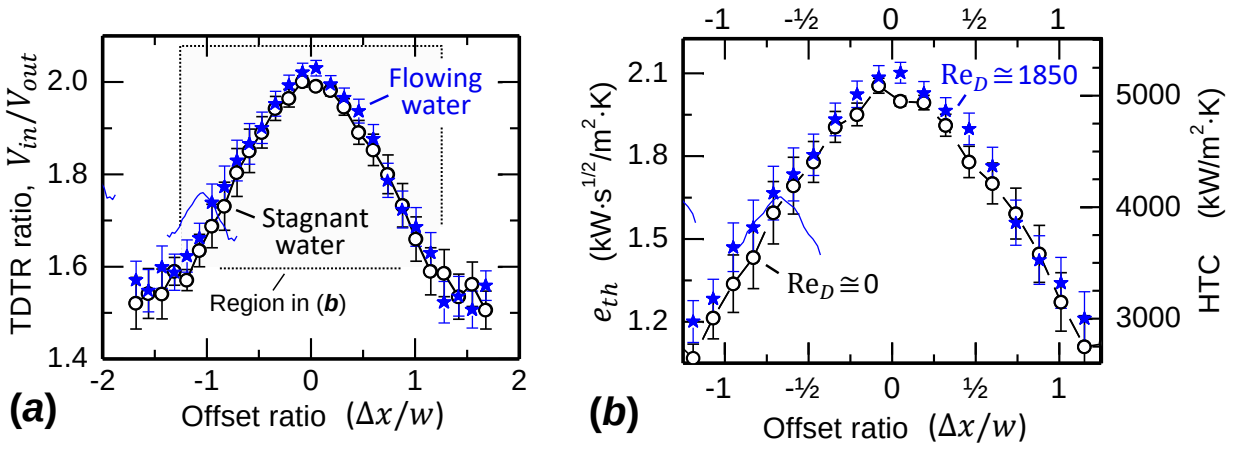

Figure 4-10 (a) Anisotropic TDTR measurements for Hf80-coated glass with flowing or stagnant water in the microchannel. (b) Corresponding thermal effusivity of water (left axis) and HTC (right axis) based on differential TDTR analysis scheme ($\tau_d = 100\,ps$, $f_{\mathrm{mod}} = 976\,KHz$, $w = 8.7\,\mu m$.

alloy consisting of Hf, Gd, and HyMu80 alloy (which we call Hf80 due to its highest Hf content). This Hf80 metal alloy not only has a low thermal conductivity (e.g., $\Lambda \cong 5.6$ W/m·K), but it is incredibly robust, facilitating later TDTR studies of flow boiling and jet-impingement with extreme hot-spot heat fluxes. The APPENIX A provides additional information and TDTR results for water and air in contact with these NbV and Hf80 alloy thin-films on FS substrates.

Figure 4-10 shows anisotropic TDTR results for Hf80-coated FS substrates with both stagnant and flowing water in the microchannel. In comparison to the Ti thin-film data, this TDTR ratio data with the Hf80 thin-film has considerably more measurement error, especially at pump-probe offsets (Δx) greater than one pump beam waist (w). For this reason, only analysis results for e_{th} and HTC are shown in Figure 4-10 (b) for the boxed-region in Figure 4-10 (a). This magnified view also helps show that high-Re flow in the microchannel influences the TDTR ratio, especially with concentrically-focused pump-

probe beams (i.e., $\frac{\Delta x}{w} \approx 0$). Similar to the results with a Ti metal thin-film (Figure 4-8), a maximum increase is observed in the TDTR ratio (or HTC) when "probing" within the developing thermal BL (i.e., probing within $0 < \frac{\Delta x}{w} <$ 1/4, which is ≈1–2 μm down-stream the center of the pump induced hot-spot).

For reference, the incident pump laser powers on the Ti (Figure 4-8 and Figure 4-9) and Hf80 (Figure 4-10) metals were both ≈ 10.5 mW. This corresponds to average hot-spot heat fluxes into the fluid of $\bar{q}_{\mathrm{Ti}} \approx 837\ W/cm^2$ and $\bar{q}_{\mathrm{Hf80}} \approx 934\ W/cm^2$, where $q_{\mathrm{CHF}} \approx\ 1000\ W/cm^2$ is a common CHF value for sub-cooled boiling on uniformly heated surfaces with water [91]. And thus, as expected, we can easily induce vapor bubble nucleation with more focused or increased laser power beams. On this note, we observe significantly improved TDTR signal-to-noise ratios by increasing the pump-probe laser powers (which would seem beneficial for the Hf80 studies in Figure 4-10). However, at laser powers ≳ 20 mW, we chaotically observed either (*i*) vapor bubble nucleation and growth at the pump-induced hot-spot or (*ii*) V_{in}/V_{out} ratio data (in the absence of bubble nucleation) that required TDTR model fits with exaggerated thermo-fluid properties. This chapter is focused on validation of the proposed technique with single-phase fluids, so laser powers < 20 mW were used. Again, the Hf80 results are provided because this metal thin-film material is stable at high heat fluxes, which is favorable for the two-phase studies of hot-spot boiling in cross-flow in the next chapter or jet-impingement boiling for the future experiments. The results and discussion on how vapor bubble nucleation and growth influence the anisotropic TDTR measurements (or the HTC measured) are discussed in the chapter CHAPTER 5:.

4.5 HTC enhancement and decomposition

In the previous sections, it was shown that the Anisotropic TDTR method can be used to measure (or predict) the local HTC. In particular, the local HTC around a micron-sized hot-spot with and without forced convection. However, the predicted HTC values are an order of magnitude greater than the maximum HTC values observed by others (see, for comparison, the single-phase HTC data in Table 2-1). In hindsight, this is expected because the TDTR method characterizes the HTC over very small length-scales (e.g., $2w \approx$ 19 μm and $\ell_{th} \approx$ 225 nm), where it is well known that the HTC is inversely proportional to the thermal BL thickness, which is also dependent on the size of the heat source [92]. Correspondingly, this length-scale correlation with the HTC is reflected by the Nusselt number, $\mathrm{Nu} = hL_c/\Lambda_f^{\mathrm{tBL}}$, where Λ_f^{tBL} is the fluid's thermal conductivity within the thermal BL (tBL) and L_c is a characteristic length dictated by the cooling/heating configuration (e.g., heater width, length, and pipe diameter, etc.). Below it is shown that the proposed local HTC measurements can be predicted by combining well-established and experimental-specific Nusselt number correlations.

For the experiments, we predict the local HTC to follow:

$$h = h_0 + h_\uparrow = \frac{\Lambda_f^{\mathrm{tBL}}}{2w}[\mathrm{Nu}_0 + \mathrm{Nu}_\uparrow] \tag{4-9}$$

where the characteristic length is diameter of the hot-spot ($L_c = 2w$) and we separate the HTC (Nusselt number) into two components. The first component, h_0 (Nu_0), represents the local HTC for stagnant water in a TDTR experiment – i.e., that associated with mainly heat conduction and some natural micro-convection. Whereas, the second component,

$h_{\uparrow}$ ($\mathrm{Nu}_{\uparrow}$), represents the local enhancement in the HTC due to increased micro-convection caused by the flowing fluid over the hot-spot. Explicitly, the following expressions is used for each component:

$$\mathrm{Nu}_0 = \frac{2w}{\Lambda_\mathrm{f}} \left(2\pi f_\mathrm{mod} \Lambda_\mathrm{f} \mathrm{C}_p^\mathrm{f}\right)^{1/2} \tag{4-10}$$

$$\mathrm{Nu}_{\uparrow} = \overline{\mathrm{Nu}}|_{(80)} \cdot N(\bar{\epsilon}, \sigma^2) \tag{4-11}$$

$$\mathrm{Nu}_{\uparrow} = \mathcal{C}\, \mathrm{Re}_D^{0.64}\, \mathrm{Pr}^{0.38} \left(\frac{\mu_\infty}{\mu_\mathrm{tBL}}\right)^{0.25} \left[\frac{1}{\sqrt{2\pi}}\, e^{-\frac{1}{2}\left(\frac{\Delta x}{w} - 0.25\right)^2}\right] \tag{4-12}$$

where the stagnant-fluid component (equation (4-10)) is purely based on the TDTR experimental conditions (see, equation (4-7)) and the forced-convection component (equation (4-11)) is based on the product of the normal distribution ($N(\bar{\epsilon}, \sigma^2)$) and the pioneering Nusselt number correlation by Incropera et al. [93] for single-phase convective heat transfer in a rectangular channel with a flush mounted square heater (hence, the subscript (80) with $\mathcal{C} = 0.13$). For the normal distribution in equation (4-12), $\sigma^2 = 1$ (i.e., a variance of w) and slightly downstream expectation (i.e., $\bar{\epsilon} = \frac{\delta x}{w} = 0.25$) are used to account for our anisotropic HTC observations with flowing fluids. Separating the Nusselt number into two components (i.e., one “constant” stagnant-fluid component and another “functional” forced-convection component) is quite common [78]. However, usually the stagnant-fluid component is an additional fitting parameter while, for TDTR, it is directly measured (and/or it has an explicit expression). It should also be noted that, in principle, additional terms could be added to equation (4-10) to account for boiling, evaporation, or chemical reactions.

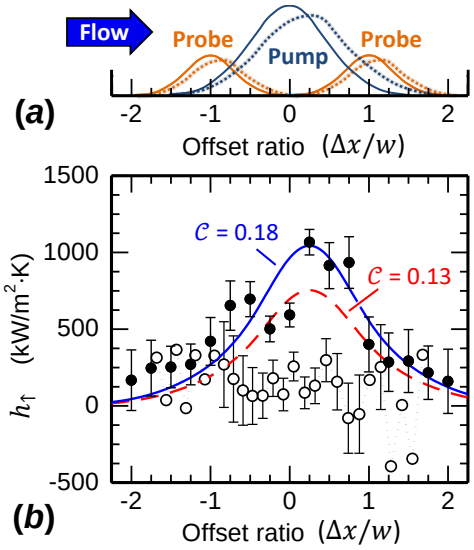

Figure 4-11 (a) Schematic of probing up- or down-stream the pump induced hot-spot in the microchannel, where the dotted-lines represent the flow-induced anisotropic metal wall temperature. (b) Comparison between the measured (symbols) and predicted (lines) enhancement in the local HTC due to forced convection over the hot-spot in the microchannel for Ti/FS (filled-circles) and Hf80/FS (open-circles).

Figure 4-11 compares the measured enhancement in the HTC (i.e., $h_{\uparrow}^{\mathrm{TDTR}} = h_{\mathrm{flow}} - h_{\mathrm{stag}}$) to the HTC enhancement predicted (i.e., $h_{\uparrow}^{Equation\ 4-9}$) due to high-Re water flow over the hot-spot in the microchannel. The lines are the predictions and the symbols are our measured data for the two different metal thin-films studied (Ti: filled-circles, Hf80: open-circles). Fair agreement is found between the Ti thin-film HTC data and the Nusselt number predictions using $\mathcal{C} = 0.18$ [92]. A maximum enhancement in the HTC is observed at a location slightly down-stream the center of the pump hot-spot (e.g., a down-stream distance of $\Delta x \approx 5 \pm 3\ \mu\mathrm{m}$ (or $\Delta x/w \approx 0.52 \pm 0.32$), which also represents the presumed region of rapid thermal BL growth). The Hf80 thin-film data does not exhibit a systematic HTC enhancement peak and that, combined with the increased measurement noise for Hf80, has led to poor correlations with the Nusselt number predictions. The Hf80

data also shows negative HTC enhancements for downstream probing at $\Delta x/w \gtrsim 1$, where negative values of $h_{\uparrow}$ corresponds to the fluid heating the metal. Nevertheless, aside from this fluid heating effect with Hf80, the anisotropic TDTR studies with both metal thin-films demonstrate that there is an overall HTC enhancement due to forced convection (especially for up-stream probing, where the flowing fluid can only cool the metal in the "probe measurement ROI").

If in-plane thermal transport in the metal is not significant, then both metal thin-films are expected to yield the same local HTC enhancement results because the flow-field conditions were identical ($\mathrm{Re}_D = 1850$, $T_{\mathrm{f}}^{\mathrm{inlet}} = 25°\mathrm{C}$). This is pointed out because the flowing water is expected to both cool and heat the metal thin-film wall of the microchannel (e.g., up-stream cooling and down-stream heating of the metal wall relative to the central pump-induced hot-spot). This is depicted in Figure 4-11 by the skewed pump and probe heating distributions (dotted-lines). Thus, the overall thermal energy exchange between the fluid and the metal heater/thermometer is dictated by both the thermal effusivity of the metal and thermal effusivity of the fluid. For reference, $e_{th}^{\mathrm{Ti}}/e_{th}^{\mathrm{water}} \approx 4.3$ and $e_{th}^{\mathrm{Hf80}}/e_{th}^{\mathrm{water}} \approx 2.0$, indicating that the Hf80 metal will conduct less in-plane heat from the hot-spot (relative to Ti); and thus, Hf80 metal will see more in-plane heat from the flowing fluid (relative to Ti). Current HTC (or Nu) predictions (using equations (4-10) to (4-12)) do not account for thermal effusivity of the metal. In addition, a Gaussian-profile assumed for the metal wall temperature. Therefore, improved experiments and predictions would benefit from both (*i*) continuum-level modeling of the metal wall temperature at different flow rates and (*ii*) additional anisotropic TDTR experiments at longer pump-probe delay times (e.g., both $\tau_d = 100\,ps$ and $\tau_d = 3\,ns$, as

shown in Figure 4-6). The former would improve our estimates of the local model parameters (e.g., Re_x, Pr_x, μ_x, Λ_x, etc.) while the latter would help decipher the relative heating or cooling contributions at different pump-probe offsets.

CHAPTER 5: TWO PHASE HEAT TRANSPORT USING TDTR

5.1 Introduction

Micro and nanoscale phase change heat transport has become an active research area in thermal sciences because of the applications [94] in microelectronics [95,96], datacenters [97,98], energy harvesting and conversion [99] , and many other technologies requiring high heat flux cooling [100]. Substantial research has been done recently on the dynamics, heat transfer, and applications of nucleate boiling at the microscale as the major phase change heat transport mechanism. Despite this, there have been challenges in physical understanding of the phenomena [59,101] and development of new theories for high heat fluxes. Hypothetical proposed models also cannot be validated [102] experimentally at high heat fluxes especially at the single bubble level mainly due to lack of high resolution techniques and measurements [103]. The reason for this is complexity of the coupling of mass, momentum, and energy transport at the solid-liquid-vapor interfaces over multiple time and length scales [60,104,105]. For example, highly variable wetted or dried areas, microlayer thicknesses, temperature and flow fields, and surface heat fluxes are created within a few micrometers by coupled yet seemingly random or chaotic events during the boiling process including vapor bubble nucleation, growth, and bubble departure or release at different frequencies. During which heat transfer mechanisms coupled to conduction, convection, phase-change, and radiation are present with variable contributions of each during the process. Moreover, all these contributing mechanisms take place in a very short time (e.g., μs) because of transient nature of the

events, and this along with transient conduction in the substrate and convection in the external flow makes the physics more difficult to predict. Deciphering all the contributions individually for each event by local measurement of heat transport across interfaces with enough spatiotemporal resolution would be extremely challenging to achieve, if not impossible. This would also require calculation of individual heat transfers by mechanisms in solid, liquid, and vapor mediums and then their contributions to the overall heat flux or heat transfer coefficient (HTC). Surface heat flux is usually estimated using heater and lost heat flux and geometrical parameters [106]. Wall temperature is traditionally measured using contact temperature sensors of thermocouples, RTDs, and significantly resolution improved versions such as microfabricated transducers array [107] or combined heater and thermistor microdevice [108]. Fluid temperature is also measured at the inlet and outlet (far from the point of interest) [109] or estimated using heat flux [103]. However, these contact based techniques are intrusive and can't predict the transient dynamics of nucleate boiling due to their long thermal response time and time constant [60].

There has also been a wide range of prior studies on CHF and HTC measurements and enhancements by different passive or active techniques including engineered fluids and nano-particles [110], textured [111], porous, or wetted surfaces [112], and applied external fields [113]. However, the basic underlying physics of heat transport mechanisms is not explained well close to CHF region in most cases, or limited to a hypothesis for a very specific case. Four active heat transfer mechanisms of microlayer evaporation, interline evaporation, transient conduction, and micro-convection, for example, are proposed based on an experimentation of FC-72 flow boiling on a microchannel

composite wall with embedded temperature sensors with 40-65 μm resolution [59]. Although improving, all these heater and sensor contact-based methods are lacking from uncertainties related to their heater and sensor sizes and configurations, and non-direct measurement of heat transport at surfaces.

Non-contact based techniques have been developed and used for both surface and fluid temperature measurements recently. Infrared Thermometry(IRT) [114] or Thermal Scanning Electron Microscopy(ThSEM) for solid surface and Liquid Crystal Thermography(LCT) or combined μ-PIV and Laser Induced Fluorescence(LIF) [115] for fluid flow temperature measurements are some of non-contact methods. Other non-contact high speed imaging or phase detection techniques are also used to measure the quality and phase distribution on the surface and relate that to the heat flux [116,117] or HTC. These methods suffer at least in one of the spatial (eg. IRT), temporal (eg. ThSEM), or temperature (eg. LCT) resolutions. Furthermore, they can only measure one of the required parameters for local heat transport estimation. It would be ideal if a method can practically measure the overall local heat flux or HTC directly at surfaces and interfaces with high enough spatiotemporal and temperature resolutions. It would also help to achieve better understanding of microscale boiling phenomena and accurate models to predict and enhance HTC and CHF at high heat fluxes.

In the previous chapter, anisotropic version of the time-domain thermoreflectance (TDTR) as a non-contact and high resolution method was used to measure the local HTC at the interface of a locally heated 60 nm Titanium layer and single phase flowing water in a microchannel. Also, it has been shown that the cooling rate of a metal wall is dictated by the thermal effusivity (e_{th}) of its surrounding materials. A differential TDTR

measurement approach was proposed to measure the convective HTC as a function of thermal effusivity of the flowing fluid in the heated and close to the wall areas [118,119].

Here the differential TDTR technique is extended to measure local two-phase heat transport in a microchannel with modifications in the data acquisition system to cover transient nature of the pool or flow boiling heat transport and transient conduction in substrate. Measurements are first done at different laser beam powers up to 40 mW (or equivalent localized heat fluxes up to 6 KW/cm^2) for both stagnant and flowing fluid cases to determine the required heating power for the subcooled boiling region of interest for transient experiments. Transient local heat transport is then characterized during all the boiling events including onset of bubble nucleation, bubble growth, departure and release for both pool and flow boiling and HTC is calculated using the measured data.

5.2 Measurement procedure and experiment modifications

Figure 5-1 illustrates the experimental test stage (a) and the concept behind the physical theory used in this investigation (b). The sample test stage comprises a 400 µm thick PDMS (Polydimethylsiloxane) rectangular ring, 70 nm of a metal alloy film sputter-deposited on a 1-inch diameter Fused Silica (FS) substrate at the bottom, and an Acrylic holder on the top. By pressing the Acrylic substrate to the FS substrate and taking advantage of the sealing property of PDMS ring the microchannel is assembled with no leakage. Optical transparency of both Acrylic and FS substrates provides the possibilities of high speed imaging of microchannel flow from top and transmitting incident TDTR laser beams from bottom sides respectively. They both have relatively low thermal conductivity

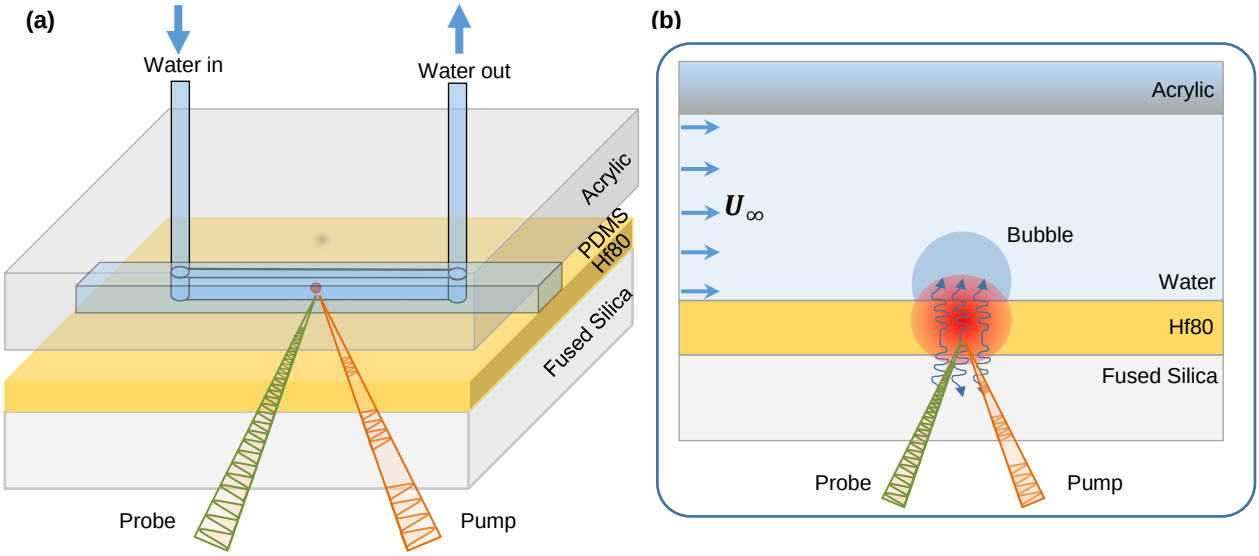

Figure 5-1 Experimental Setup. (a) Schematic of the sample stage consisting of Acrylic holder, PDMS microchannel, 70 nm of Hf80 alloy deposited on a Fused Silica substrate. (b) Cross-sectional view of the water flow in microchannel. Modulated pump beam heats FS, Hf80 and water in the red region and a single bubble nucleates and grows.

and act as insulators too. The metal film is Hf80 which is explained in the previous chapter.

5.3 Localized HTC map of pool and flow boiling curves

Boiling curves which relate transferred heat flux of the wall to fluid and the wall superheat are traditionally used to describe different boiling flow and heat transfer regimes [78]. They also facilitate to have an estimate of critical heat flux (CHF) and device burnout limits [120]. Internal two-phase flows inside microchannels show different boiling regimes, depending on the relative size of bubbles to microchannel dimensions and quality of the flow which make them more complicated than macrochannel or external flow boiling heat transfer. It's mainly because the vapour can't escape to a free surface

and is forced to mix and flow along the channel with fluid. Most of the curves in the literature for internal two-phase flows show flow and heat transfer patterns starting from subcooled region and developing to bubbly, slug, annular, transition, and mist flows along the channel as the fluid is heated by continuous heat loads. measurements are also based on averaged-over-heater values traditionally. However, the key to understanding the heat transfer interaction of the mixed vapor bubbles and liquid flow with the wall at each section of the microchannel is to investigate the thermal behaviour of a single bubble individually in the same heat flux or wall superheat regime. A detailed study has investigated local heat transfer mechanisms at the single bubble level for isopropanol and FC-3284 fluids using micro-optical and -thermocouple probes (tip diameters of ~1.5 and 16 μm). It's concluded that temperature of the bubble's vapor increases from low flux nucleate boiling to film boiling regimes along the entire boiling curve [121]. Also, it has been shown that CHF of pool boiling increases with increase in subcooling level of bulk fluid or decrease in gravitational acceleration [122]. The model proposed for nucleate boiling HTC by Stephan [123] reveals that the maximum heat flux in the microlayer of the micro-region on the three-phase contact line is two orders of magnitude higher than the CHF of macroscale boiling curves. They also found that evaporation is the main mechanism of heat transfer in this region. However, it's only validated with mean and time independent data because of lack in experimental resolution.

A series of steady state TDTR measurements are done here before moving on to the transient experiment. The purpose is first to reconstruct the local pool and flow boiling curves for just a single bubble in terms of HTC in the same experimental conditions for both pool and flow boiling. It will also determine the right laser power or heat flux to start

bubble formation in the subcooled boiling regime for transient measurements. The probe power is fixed at 4 mW and the pump power varies from 10 to 50 mW with 5 mW increments. These are laser powers before the objective and after 25% power loss through the 20x objective the total laser power range on the sample would be 10.5 to 40.5 mW. It should also be noted that only 40% of this power absorbed to the Hf80 film because of its reflectivity of R_{Hf80}=0.6 which will be considered for calculations later. However due to the small focused beam waists of pump w_{pump}=9.5 μm and probe w_{probe}=7.5 μm the applied heat flux ranges from q=2 to 6 Kw/cm^2.

Measurement procedure is such that first validity of the experimental setup and accuracy of the measurements are confirmed by running two full TDTR scans with stagnant air and water in the microchannel respectively. Then at $\tau_d = 100\, ps$ delay time between the pump and probe beams in-phase and out-of-phase are recorded for stagnant fluid after both pump and probe beams unblocked simultaneously and the signal reaches an average constant value. Beams are blocked then to let the fluid and the sample back to room temperature and initial condition for the next measurement with flowing fluid. This procedure is repeated after each pump beam power increase until the maximum applied heat flux.

Measured in-phase, out-of-phase, and their ratio for stagnant and flowing fluids vs the laser power are shown in Figure 5-2. Magnitudes of V_{in} and V_{out} in both stagnant and flowing fluids increase linearly with close rates until the laser power of ~26 mW, where the fluid remains single phase yet. The reason for this increase is not just simply more reflected power since the probe power is filtered down to a constant value of 80 μW on the detector. However, since the signal is a product function of intensity of the reflected

probe beam and surface temperature change [62] the in-phase and out-of-phase components of the signal also increase as the surface heated more intensely. The ratio also increases slightly in this range which indicates the augmented cooling rate at higher heat fluxes. It should also be noted that at lower heat fluxes there is no apparent difference between stagnant and flowing fluid ratios which will be discussed later in this section.

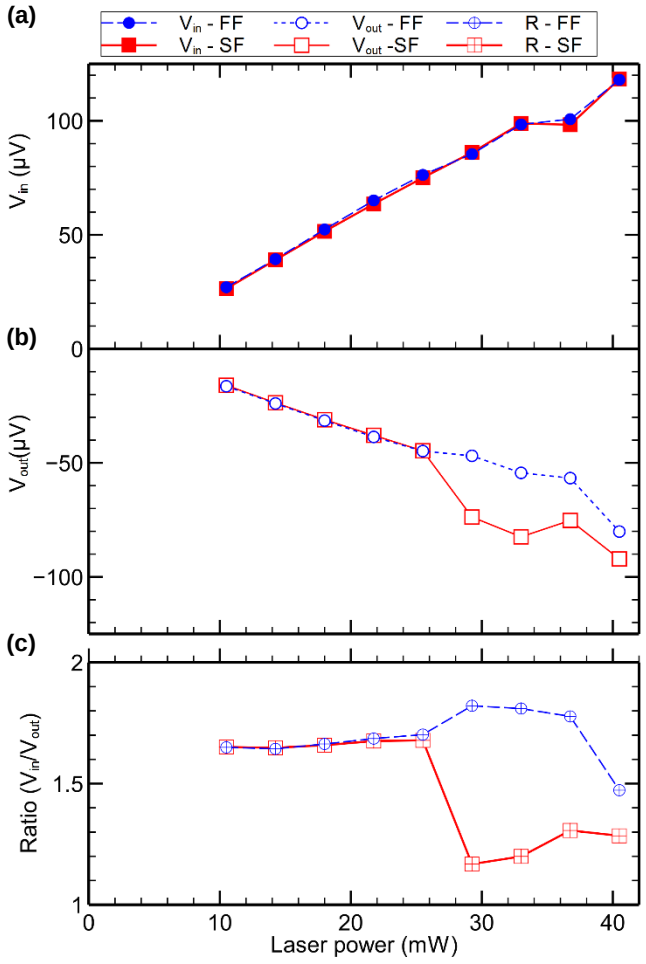

Figure 5-2 Measured steady state TDTR data. (a) In-phase, Vin (filled symbols), (b) out-of-phase, Vout (open symbols), and (c) the ratio, Vin/Vout (plus symbols) at different laser powers for steady state stagnant fluid, SF (red squares) and flowing fluid, FF (blue circles).

Beyond 26 mW in-phase follows similar trend as before for both stagnant and flowing fluids. This is while a separation in the out-of-phase between stagnant and flowing cases occurs after this point, where bubble nucleation starts as it can be seen on the camera. With further laser power increase bubble grows faster and bigger and out-of-phases get more separated for stagnant and flowing fluids and finally approach to re-join. From these observations one can guess that in-phase and out-of-phase represent sensible and phase change contributions of the heat transport respectively.

To calculate the local HTC from the measured ratios on the spot thermal conductivity and volumetric heat capacity of the fluid are extracted by solving diffusion equation bidirectionally in cylindrical coordinates through a multi-step differential TDTR analysis scheme[119]. This could be done in two methods. First, like what we have done in our past works heat capacity of the fluid is considered a constant number (at room temperature) and the model fitting is done by varying thermal conductivity. In the second method, both fitting parameters are considered variables as temperature and phase change. The first one is convenient for single phase flow and the second one is more realistic for phase change heat transport since it models heat capacity of vapor as well. However, the results for both methods are same as their product in terms of thermal effusivity is the ultimate modelling parameter which determines cooling rate of the fluid.

These results are depicted in Figure 5-3 which shows effusivities are same when obtained using either of methods, ie variable Λ_w and constant C_w (open markers) or variable Λ_w and C_w (filled markers) for both stagnant (red squares) and flowing (blue circles) fluids. Separate plots of Λ_w and C_w and more details are in the APPENDIX A. These curves have similar trends as their corresponding ratio plots in Figure 5-2 (c). It

starts with almost same effusivites for stagnant and flowing fluids at lower heat fluxes (part A) because in this single phase region cooling capacity of stagnant water by natural convection is enough to remove heat from the wall surface under thermal boundary area. Furthermore, flow effect can't be seen effectively on the thin thermal boundary layer very close to the wall where velocity approach zero because of no-slip condition. From the heat flux of 2.5 to 3.5 kW/cm^2 (part B) the ratio for the flowing fluid increases slightly more than that for the stagnant one because thermal boundary layer expands more and it feels the convection effect deeply. Distinct flow effect on heat transfer enhancement is observed with increased heat flux (part C2). This part has the same heat flux as the region in the stagnant fluid where bubble nucleation occurs (part C1) however a few degrees more cooling by the flow prevents the bubble from nucleation and growing. There is a chance of tiny bubbles nucleation right on the focused laser spot but they're washed away quickly by the flow as soon as they appear. Hence, we call it "Enhanced forced convection and μ-nucleation", where the maximum cooling rate is measured.

A bubble grows very fast and a layer of vapor forms in the microchannel beyond the critical heat flux of ≈4.5 kW/cm^2 for the stagnant fluid case upon unblocking the TDTR laser beams which is known as film boiling (part D1). Again, at the same heat flux level if we let the fluid flow in the microchannel we'll see a different heat transfer regime, ie nucleate flow boiling, as illustrated in Figure 5-3 (part D2). This algorithm of flow-assisted regime-shifted heat transfer enhancement happens again here as the flow helps to shift film boiling regime one step back to nucleate boiling for the same heat loads but at higher cooling rates. It shifted stagnant nucleate boiling (C1) to the enhanced forced convection

and μ-nucleation (C2) before. So, flow augments thermal transport mainly by changing heat transfer mechanism.

Figure 5-3 provides a broad spectrum of local single and two phase cooling rates (ie thermal effusivity) for different flow and heat transfer regimes. However, it would be more useful in terms of practical aspects and application if its variables, effusivity and local heat flux, could be converted into widely used parameters such as HTC and wall temperature or superheat, respectively. Empirical correlations between hot spot temperature and local HTC would be beneficial Specially for future high flux hot spot thermal management [124].

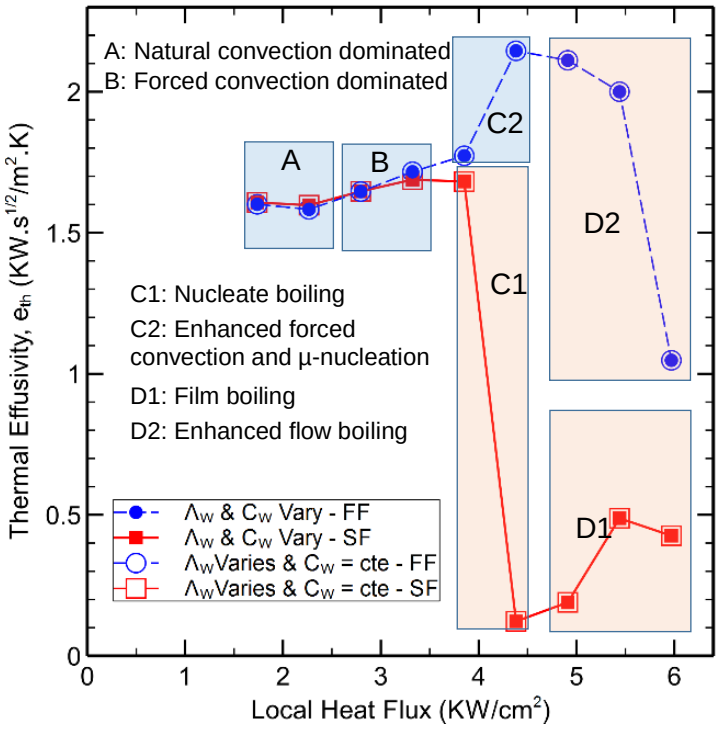

Figure 5-3 Obtained thermal effusivities from TDTR data and model as a function of local heat flux using two methods, variable Λ_w and constant C_w (open markers) and variable Λ_w and C_w (filled markers) for both stagnant (red squares) and flowing (blue circles) fluids. Results for two methods are identical.

A bubble grows very fast and a layer of vapor forms in the microchannel beyond the critical heat flux of ≈4.5 kW/cm^2 for the stagnant fluid case upon unblocking the TDTR laser beams which is known as film boiling (part D1). Again, at the same heat flux level if we let the fluid flow in the microchannel we'll see a different heat transfer regime, ie nucleate flow boiling, as illustrated in Figure 5-3 (part D2). This algorithm of flow-assisted regime-shifted heat transfer enhancement happens again here as the flow helps to shift film boiling regime one step back to nucleate boiling for the same heat loads but at higher cooling rates. It shifted stagnant nucleate boiling(C1) to the enhanced forced convection and μ-nucleation (C2) before. So, flow augments thermal transport mainly by changing heat transfer mechanism.

Figure 5-3 provides a broad spectrum of local single and two phase cooling rates (ie thermal effusivity) for different flow and heat transfer regimes. However, it would be more useful in terms of practical aspects and application if its variables, effusivity and local heat flux, could be converted into widely used parameters such as HTC and wall temperature or superheat, respectively. Empirical correlations between hot spot temperature and local HTC would be beneficial Specially for future high flux hot spot thermal management [124].

5.3.1 Hot spot temperature

One of the advantages of the TDTR technique is that the heated wall temperature under the focused laser power could be predicted using a stablished correlation and the applied heat flux and the wall surface and thermal properties. That correlation is just for the sample in contact with air. In my measurements, which the sample wall is in contact

with fluid, the correlation is modified and thermal conductivity of the fluid (obtained from the TDTR model) is incorporated to take the cooling effects of the fluid into account. The final form of the hot spot temperature T_{HS} is as:

$$T_{HS} = \frac{P_{Laser}(1-R)}{2\sqrt{\pi}w} \times \left(\frac{1}{\Lambda_f + \Lambda_{sub}}\right) + T_{amb} \quad (5\text{-}1)$$

in which P_{Laser}, w, R, Λ_f, Λ_{sub}, T_{amb} are laser power, beam waist, surface reflectivity, fluid thermal conductivity, substrate thermal conductivity, and ambient temperature. Λ_f in the above equation was obtained using the ratio data and the second fit method (discussed previously). Λ_{sub} is also calculated in an iterative method to have the most accurate temperature dependent thermal conductivity.

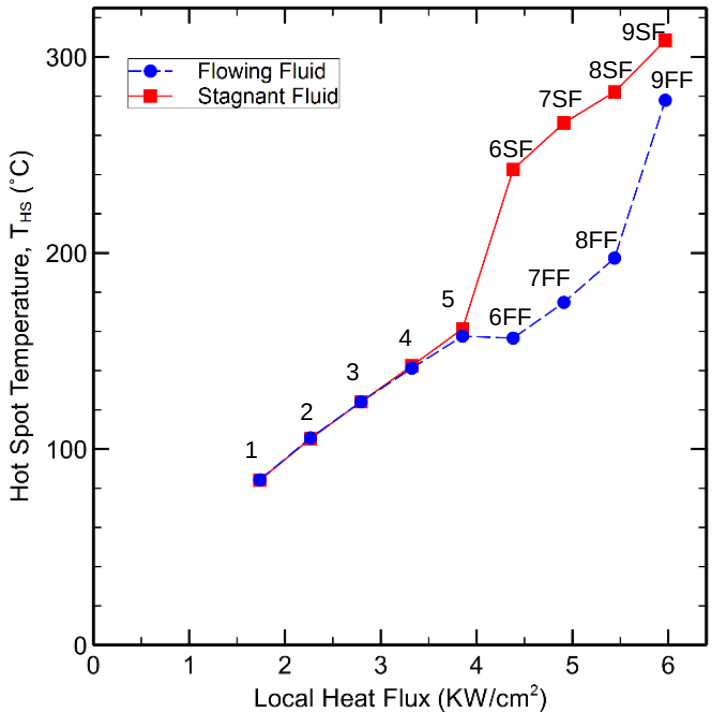

Figure 5-4 Hot spot temperature. Temperature of the heated surface area by the laser on Hf80 wall (hot spot temperature, T_{HS} (˚C)) of single and two phase stagnant (red squares) and flowing (blue circles) fluids in microchannel as a function of local heat flux.

The result of hot spot temperature vs local heat flux is shown in Figure 5-4. As the cooling rate for stagnant and flowing fluids were same until 3.3 KW/cm2 (point 4), there is no apparent difference between their hot spot temperature too as it's expected. After this point for the next measurement flux (point 5) we see about 4 ˚C cooling by flow for the single phase flow. We see T_{HS} separation for stagnant and flowing fluids at $T_{HS} \approx 161$ ˚C which means boiling occurs at this point. This temperature is too higher than typical temperature for the onset of nucleate boiling (T_{ONB} ~104 ˚C) and shouldn't be interpreted as T_{ONB}. With the knowledge that we measure average and steady values here we notice that the measured temperature for stagnant fluid represents center of the bubble's temperature on the wall at the last stage of bubble growth. The heat flux at this point can be considered as the CHF for pool boiling. It's the temperature of the dry spot, ie a small portion on the bubble's base surface, right on top of where the focused laser beam heats and when the bubble is fully grown. In these conditions, there is lesser amount of heat transfer by evaporation at the bubble's center on the dry spot than three-phase contact line at sides which makes temperature rise of the dry spot faster. Dry spot temperatures up to $T_{HS} \approx 149$ ˚C inside water bubble were reported by Dhillon et al. [111] at 180 W/cm^2 heat flux on a 650 µm thick Si surface µ-structured with 10-µm-spaced micropillars heated by a 1 x 2 cm^2 size heater. However instead of direct surface temperature measurement of dry spot they used an approximation to obtain temperature profile of Si substrate and T_{HS} from IR thermography data.

The next point (6SF) for the stagnant fluid which has the minimum amount of effusivity (or cooling rate) shows a huge jump of 81 ˚C increase in the dry spot temperature. At this point the bubble's final size is bigger than before and there is no

cooling by evaporation neither by single phase convection (water or vapor) on the dry spot so its temperature rises quickly. On the other side, temperature of the corresponding point for the flowing fluid case at the same flux which has the maximum amount of effusivity (or cooling rate) drops down to $T_{HS} \approx 156$ ˚C which is even less than $T_{HS} \approx 157$ ˚C for the point 5 at lower heat flux. This dramatic difference of T_{HS} between 6SF and 6FF points ($\Delta T_{HS} \approx 86$ ˚C) is due to fact that heat transports from the hot surface mostly and efficiently by evaporation when the bubble starts nucleation and growing or when the hot surface rewets reversely by the flow. These two surface sweeping phenomena happen together in a reciprocating cycle repeatedly until T_{HS} drops down rapidly.

After the peak points of cooling rate (i.e. minimum and maximum at 6SF and 6FF points for stagnant and flowing fluids, respectively) the dry spot temperature increases with increase in heat flux regardless of flow or no-flow conditions. The author hypothesizes that at a specific flow rate and beyond an extreme heat flux (EHF) flow may reduce the bubble size and increase evaporative heat transfer at the liquid-vapor interface on three-phase contact line but it's unable to rewet and cool down the dry spot at the center due to EHF. It's similarly hypothesized for the dry spot temperature above CHF in pool boiling [114].

T_{HS} for SF is higher than that for FF as it's expected however their differences decrease with more intense heating and it seems they're approaching to closer T_{HS} temperatures at very high heat fluxes. We also note that T_{HS} increases along the boiling curve monotonically as it was observed for vapor temperature inside the bubble [121].

5.3.2 HTC enhancement

Now that local effusivity and hot spot temperature at each heat flux are available, we can reconstruct a local pool and flow boiling curves. We prefer HTC and T_{HS} as the more useful parameters for high heat flux applications. Our stablished differential scheme [119] is used to calculate local HTC using the obtained thermal conductivity and heat capacity (or effusivity) of the fluid form the bi-layer model and measured ratios. Local HTC enhancements are then calculated by subtracting HTC at each heating flux from HTC at the minimum applied heating flux for the stagnant fluid to see how much heat transport is augmented with flow at other heating fluxes. Results are shown in Figure 5-5 for single and two phase stagnant (red squares) and flowing (blue circles) fluids in the microchannel as a function of hot spot temperature. The graph is divided into two HTC enhancement and HTC suppression regions above and below the reference line (dotted black line) crossing the zero-enhancement, respectively.

With both SF and FF there is a HTC enhancement (a little more with FF) as T_{HS} increases from 125 ˚C to 160 ˚C in the single phase area. With the increase of T_{HS} above 160 ˚C up to ≈ 240 ˚C not only the hot spot's temperature rises very fast to the dry spot temperature range for the SF, there is no HTC enhancement and HTC drops down suddenly. This is area which should be avoided without fluid flow. The trend is completely on the opposite side with FF in this T_{HS} range where the maximum HTC enhancement is observed. At higher heat fluxes and above dry spot temperature of ≈ 240 ˚C, HTC starts falling for FF to the negative enhancements.

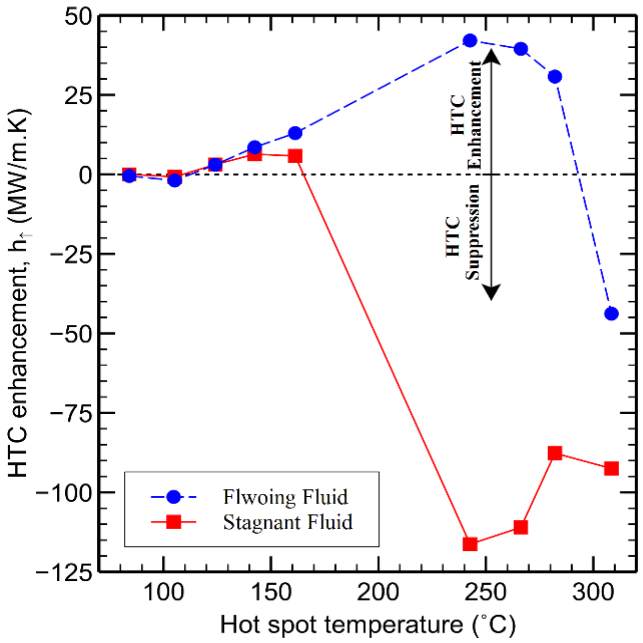

Figure 5-5 Pool and flow boiling curves by TDTR. Local HTC enhancement of single and two phase stagnant (red squares) and flowing (blue circles) fluids in microchannel as a function of hot spot temperature.

If we compare plots of effusivity vs local heat flux in Figure 5-3 and HTC enhancement vs hot spot temperature in Figure 5-5 we see that they are scales version of each other. So, all the discussions were done earlier in previous section regarding flow and heat transport regimes and mechanisms would be valid here as well.

5.4 Transient local HTC predictions using TDTR

Thermal diffusion time ($t_D = \sqrt{t_s^2/\alpha}$ in which t_s and α are tickness and diffusivity) for substrates or thin films could be as low as few µs to typically few hundreds ms depending on their tickness and diffusivity. Transient high heat flux loads can transfer instantly at these time scales and create sudden and beyond-limit temperature fluctuations and device failure. Fortunately, lifespan of a bubble nucleation, growth, and

departure or release could also range from less than 0.5 ms [108] to 50 ms [114] or even longer than 1s depending on heat and mass fluxes, subcooling level, nucleation site density, and relative bubble and geometry sizes. Those lifespan events of a bubble can be used actively to be synchronized with transient loads to suppress high temperature fluctuations and prevent boiling crisis and burnout if they're well understood.

Here we take advantage of ns temporal resolution of TDTR technique to obtain thermal temporal fluctuations and HTC of a single bubble at the center of its interface with wall during its ebullition cycle. The total laser power is chosen to be between the minimum required to start subcooled nucleation and CHF of the pool boiling, where the minimum and maximum cooling rates are observed with stagnant and flowing fluids, respectively. This range is critical since within 10% change in heating flux, flow can have dramatic effect on HTC. Bubble size reaches up to half of the microchannel height when it's fully grown at this power. So, there would be no confinement and upper wall interaction.

Differences in experimental setup for transient measurements are using a high speed (1GHz) oscilloscope to record in- and out-of- phases separately and directly from the lock-in and synchronizing it with the camera to capture frames of boiling events. Recorded V_{in}, V_{out}, and the ratio are shown in Figure 5-6. Like the steady state measurements of the ratio vs heating flux in previous section, here also V_{out} indicates phase change and boiling events while the in-phase shows small fluctuations because of ac heating and sensible heat change (5-10 ˚C). For the out-of-phase which is reflected in the ratio as well, the bottom fluctuating line shows when the bubble is fully grown, and the peaks are when the grown bubble is washed away and a new bubble is about to form.

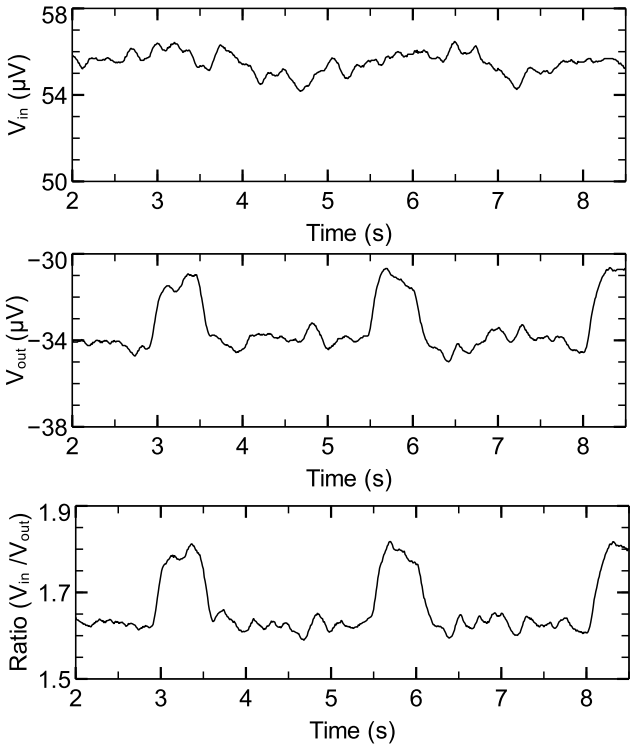

Figure 5-6 Transient TDTR measurement data. In phase (a) and out of phase (b) components of the transient TDTR signal for subcooled flow boiling of water in microchannel and their ratio (c).

The upper limit of the ratio at peaks (R~1.8) is same as the ratio at 100 ps delay time in the still-water full TDTR scan. However, the lower limit of the ratio (R~1.6 when bubble is grown) is more than that at 100 ps delay time in the air-sample full TDTR scan (R~1.4 in Figure A-3). This is because of transient cooling effect of flow and bubbles and the difference between thermal properties of the trapped vapor inside the bubble and the air.

It takes approximately 1.5 s for each bubble to be released and disappeared from the nucleation site by the flow after its full growth and this pattern is repeated for the next bubble. Other than phase change and nucleation, transient heat flux through the wall and instantaneous surface temperature changes are also reflected in the plot by the small

fluctuations. The size of fluctuations is small compared to the bubbles main peaks. Knowing that the systematic measurement errors are already included in and combined to the temperature fluctuations, makes them of less concern. However, more efforts needed to differentiate between them in measurements in order to get accurate temperature fluctuations.

5.4.1 Subcooled single bubble in pool and flow boiling

Based on our observations in transient measurements of a single bubble nucleation at a constant local heat flux we have illustrated ebullition cycle events of a single bubble and its ratio (or equivalently HTC) in the pool and flow boiling in Figure 5-7. Here are a brief list of events and related discussions:

1: Laser beams are unblocked and heating is started.

1→2: Temperature of the SF increases and heat transported by natural convection

2: A bubble starts nucleating

2→3: Bubble starts growing until it gets bigger than the beam waist.

3→4: Bubble continues growing until its maximum size at 4.

4: Fluid starts flowing.

4→5: Fully grown bubble is still there and flow tries cool down the phase contact line and liquid-vapor interface.

5→6: 3-phase contact line recedes and bubble gets smaller.

6: After few oscillations the bubble released from the surface.

6→7: the dry spot is purely covered by the single phase FF.

7: New bubble starts nucleating.

7→8: Bubble grows to its full size.

8→9: Bubble is still there under the flow.

9→ : Bubble claps, release, nucleation and growth cycle repeats

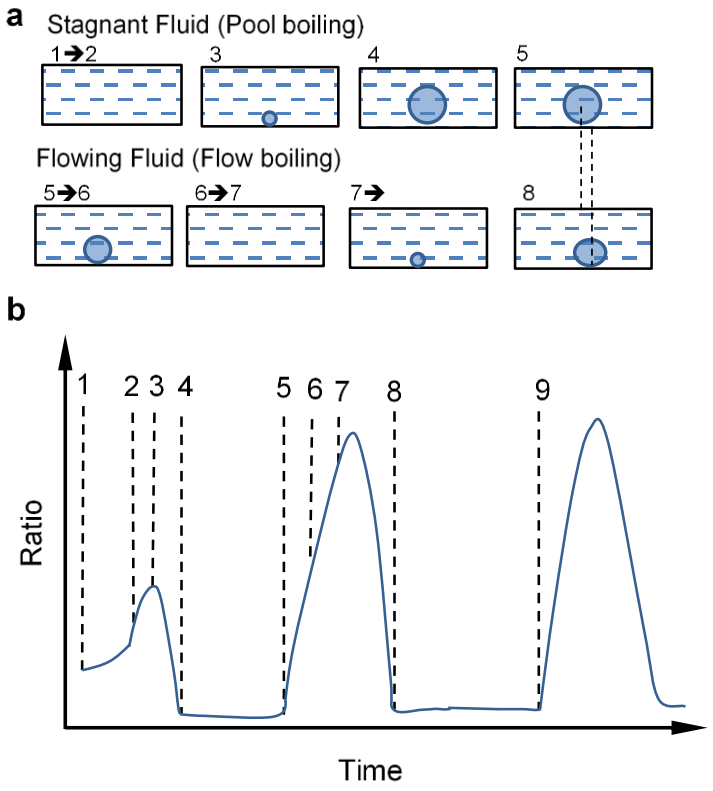

Figure 5-7 Ebullition cycle events of a single bubble. Time frame (a) and the ratio (b) of life span events of a single bubble in pool and flow boiling.

As it can be seen in Figure 5-7 flow increases ratio and enhances heat transport in several ways. It's done first by pushing the evaporating contact line toward the center of the bubble and then by covering dry spot by microlayer close to the meniscus area. It's also observed that the time it takes for a bubble from nucleation to full growth in pool boiling (2→3→4) is shorter than that in flow boiling (6→7→8). But the bubble size is

smaller with flow (8 vs 4) and its shape changes from sphere to ellipse. The center of the bubble also is shifted a little to the downstream (8 vs 5) which helps the meniscus thin area to be on or closer to the dry spot.

5.4.2 HTC predictions

The method is used to calculate transient HTC from data is basically same as steady state HTC after measurement of the ratio. Results are plotted in Figure 5-8 and a few selected data points on the plot are associated to their related time frame image on the camera. Local transient HTC follows the same trend as the ratio and as it's expected the bottom line HTC_{min} corresponds to full grown bubble and the peaks and HTC_{max} to the moment that bubble is released from the surface and the next bubble starts to form. HTC decrease when bubble grows may not seem convincing however this is justifiable considering that it's measured only at the center of the bubble (ie dry spot) not on the three-phase contact line while growing. So, whenever the flow gets closer to the dry spot and passes through it (receding or advancing) HTC increases suddenly. It means that for very hot or more specifically dry spots, continuous and small bubbles on the order of thermal diffusion time and dry spot length scales respectively could be a reliable high heat flux cooling solution. This could be achieved by controlling the bubble size and frequency through geometry and dimension, surface properties, and fluid's flow rate and thermal properties.

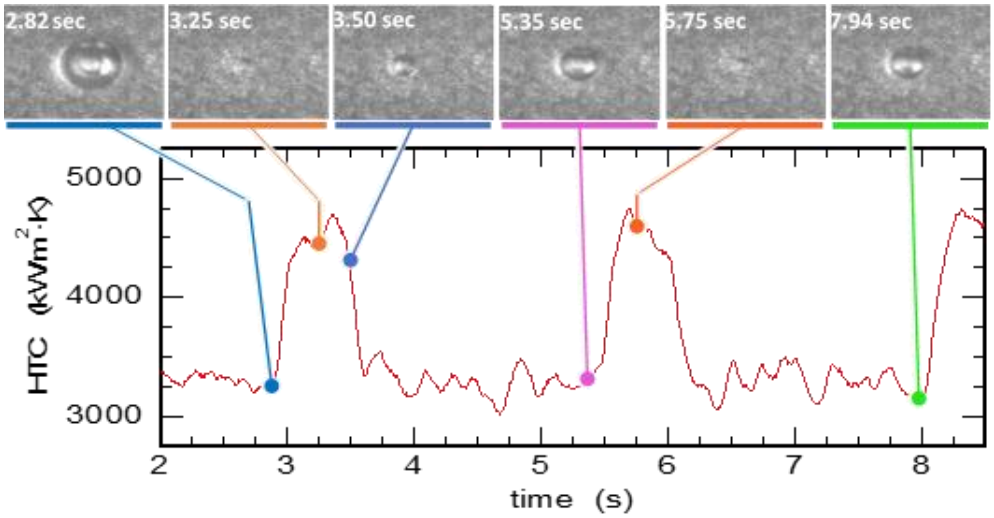

Figure 5-8 Calculated transient local HTC vs time in the cross flow microchannel by the differential TDTR scheme. Six images on the top show screenshots of the recorded video at the specified data points. Fluctuating bottom line indicates the fully-grown status and peaks show the ONB status

CHAPTER 6: CONCLUTION AND FUTURE DIRECTIONS

The anisotropic TDTR method is shown to be a useful technique for characterizing anisotropic heat transport at sub-micron length-scales. The research in this dissertation supports that the technique can be extended – via a differential measurement methodology – to characterize both the conductive and convective heat transfer contributions to fluid-flow cooling of a laser heated microchannel wall with sub-cooled water and moderate Reynolds number flow-field conditions in both single- and two-phase flows. It's shown that this local HTC measurement can be predicted (with relatively good agreement using a Ti metal thin-film heater/thermometer) using a two-component Nusselt number correlation, where the first component represents the HTC due to both heat conduction and natural micro-convection of the stagnant fluid, and the second component accounts for the HTC enhancement due to forced convection. However, the results with other thin-film heaters/thermometers having lower thermal conductivities were not predicted well by this two-component correlation, presumably due to wall heating effects by the coolant downstream the pump-induced hot-spot. In this regard, future studies would benefit from (*i*) in-situ experiments that can independently characterize the temperature distribution of the channel-wall, (*ii*) additional anisotropic TDTR experiments at multiple pump-probe delay times (e.g., both $\tau_d = 100$ ps and $\tau_d = 3$ ns), (*iii*) studies directly with microchannel-structured Si heat sinks or microchannels fabricated on ultra-low thermal conductivity substrates to maximize the net heat transferred into the fluid, and (*iv*) other wall heating configurations (i.e., eliminating the pump beam as the hot-spot heating source) such as uniform wall heating or the use of a third laser beam (for hot-spot

heating). However, the latter would limit the proposed capability of using the stagnant TDTR measurements to directly predict the HTC distribution of the stagnant fluid.

APPENDIX A:

DETAILS of TDTR MEASUREMENTS & RESULTS

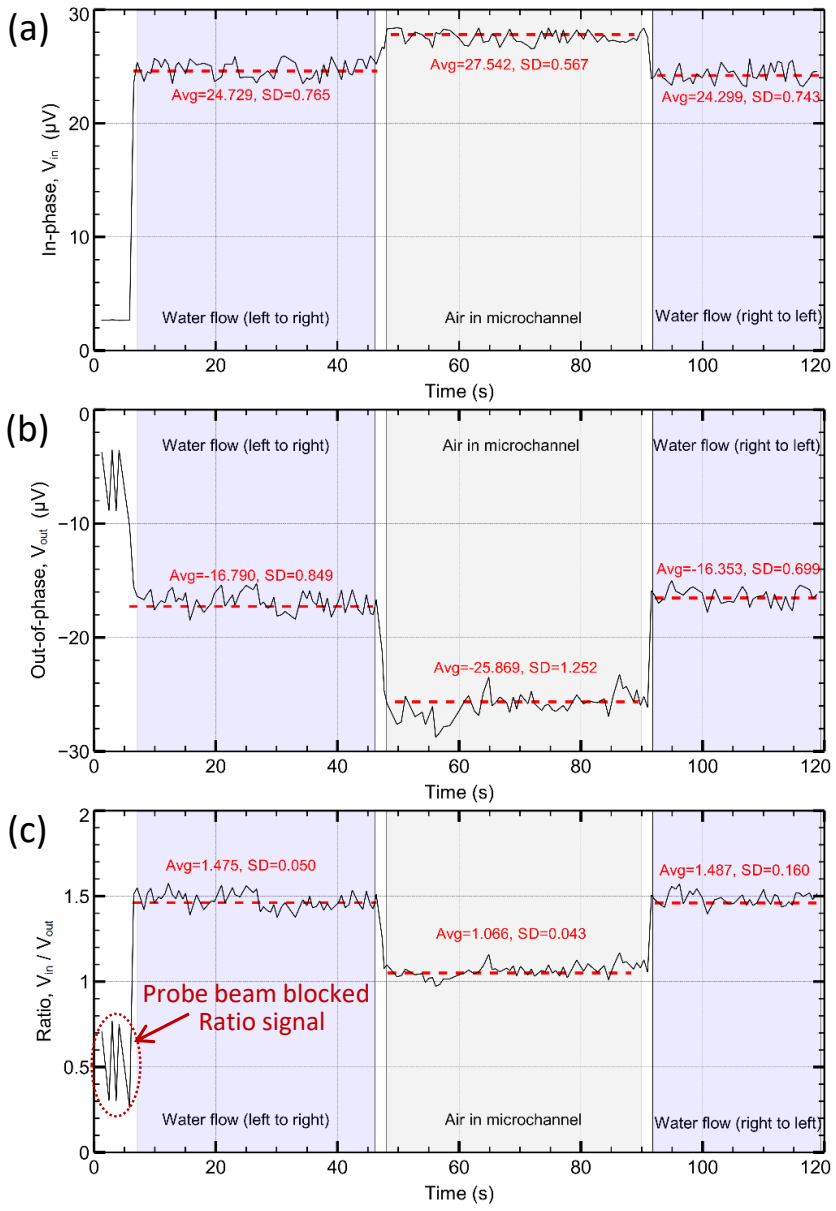

Figure A-1 TDTR in-phase (a), out-of-phase (b), and ratio (c) data as a function of time for flowing water in a microchannel using a Ti-coated FS glass window.

For example, at time $t = 0$ seconds water is flowing in the microchannel from left-to-right (respective to Figure 4-2, then at time $t \approx 46$ seconds an air bubble enters the microchannel (with the corresponding and expected change in TDTR signal), then at time $t \approx 70$ seconds the flow direction is reversed (right-to-left) causing the air bubble to leave

the microchannel at time $t \approx 93$ seconds (yielding the same TDTR data as measured with water flow in the initial flow direction). Experimental details: $f_{\mathrm{mod}} = 962\ \mathrm{kHz}$, $P_{Pump} \approx 10.5\ \mathrm{mW}$, $P_{Probe} \approx 2.8\ \mathrm{mW}$, $w_{Pump} = 8.7\ \mu\mathrm{m}$, $w_{Probe} = 6.7\ \mu\mathrm{m}$, $\mathrm{Re}_D = 1850$.

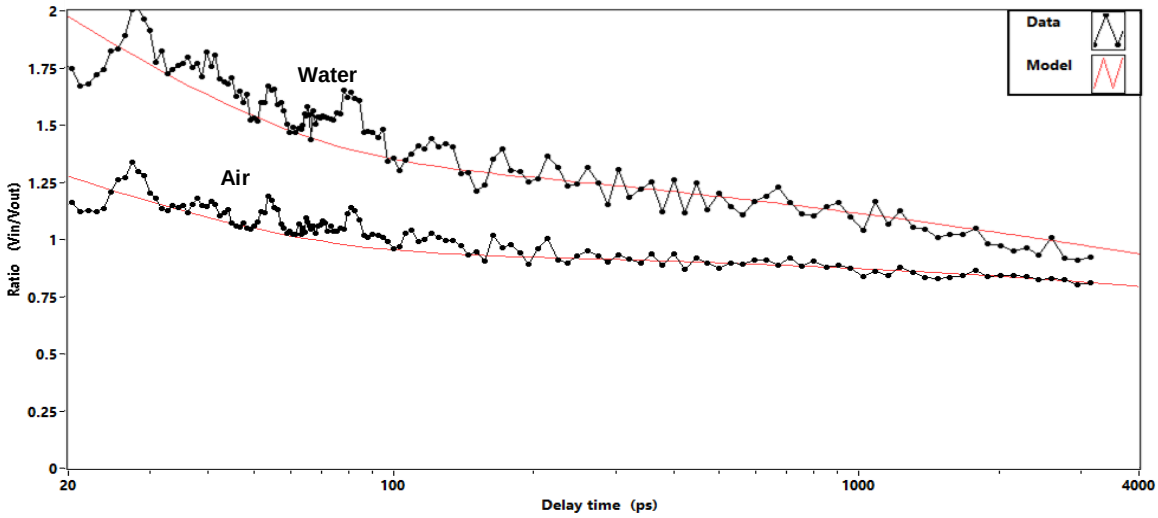

Figure A-2 TDTR ratio data (black symbols) and model predictions (red lines) as a function of pump-probe delay-time for a NbV-coated FS glass window in thermal contact with non-flowing (stagnant) water or air in the microchannel (f_{mod} = 962 kHz, $P_{Pump} \approx$ 10.5 mW, $P_{Probe} \approx$ 2.8 mW, $w_{Pump} =$ 8.7 μm, $w_{Probe} =$ 6.7 μm).

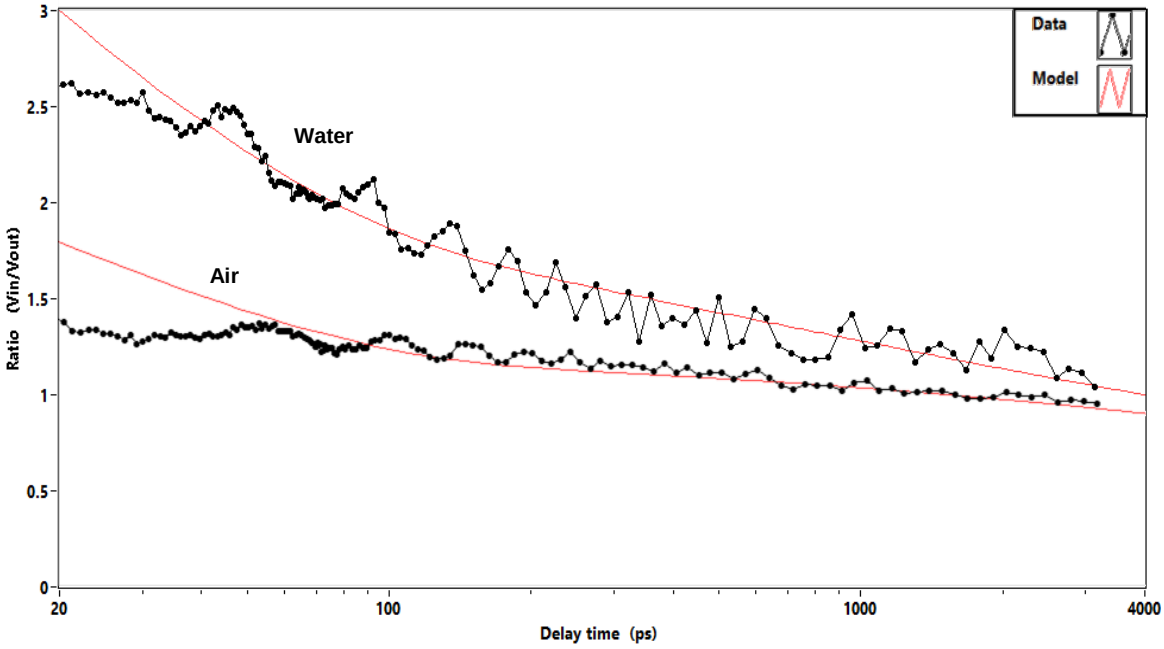

Figure A-3 TDTR ratio data (black symbols) and model predictions (red lines) as a function of pump-probe delay-time for a Hf80-coated FS glass window in thermal contact with non-flowing (stagnant) water or air in the microchannel (f_{mod} = 962 kHz, $P_{Pump} \approx$ 10.5 mW, $P_{Probe} \approx$ 2.8 mW, $w_{Pump} =$ 8.7 μm, $w_{Probe} =$ 6.7 μm).

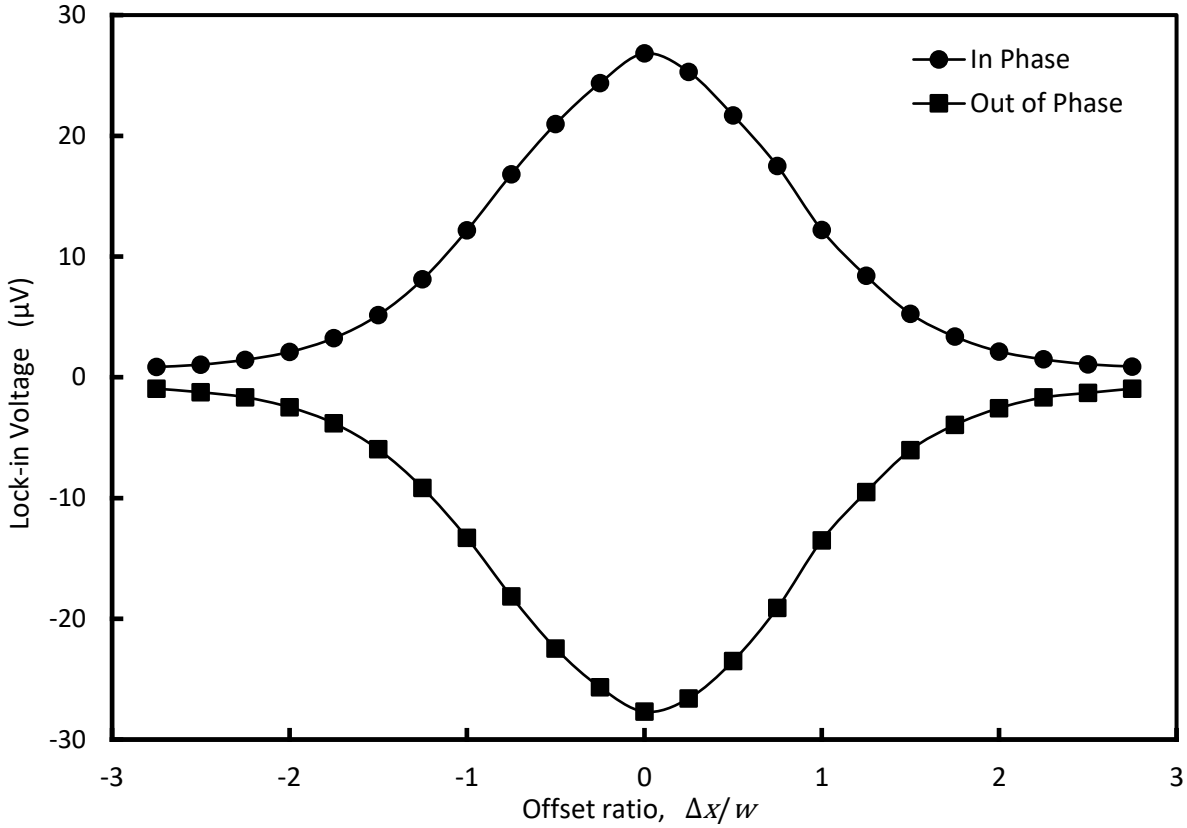

Figure A-4 In-phase (circle symbols) and out-of-phase (square symbols) components of measured TDTR voltage signal as a function of pump-probe offset ratio for a Nb0.5V0.5 -coated FS substrate in thermal contact with stagnant air in the microchannel.

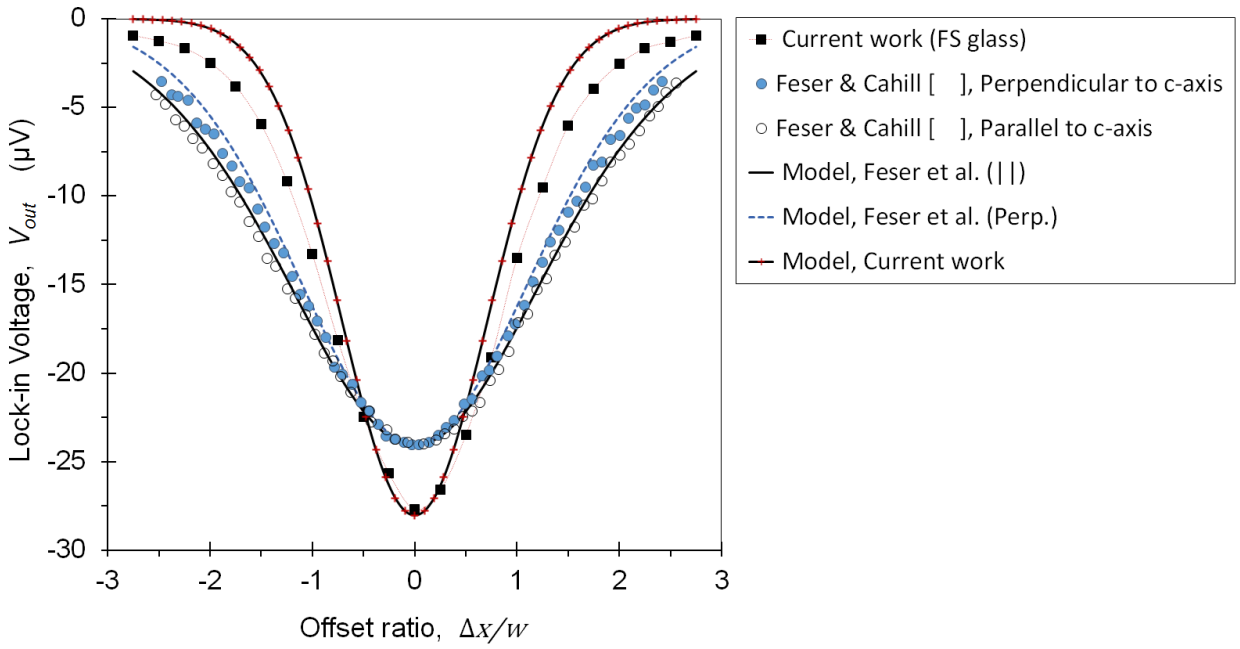

Figure A-5 Comparison between the measured (symbols) and model predicted (lines) out-of-phase TDTR voltage signal (V_{out}) as a function of pump-probe offset ratio ($\Delta x/w_{pump}$) for different glass substrates coated with a $Nb_{0.5}V_{0.5}$ thin-film alloy.

Experimental details (this work): Square symbols measured via a back-side TDTR experimental configuration using a $Nb_{0.5}V_{0.5}$ alloy deposited on a fused silica (FS) glass, where the $Nb_{0.5}V_{0.5}$ alloy is in thermal contact with stagnant air in the microchannel (f_{mod} = 962 kHz, τ_{d} = 100 ps, $P_{Pump} \approx$ 10.5 mW, $P_{Probe} \approx$ 2.8 mW, w_{Pump} = 8.7 μm, w_{Probe} = 6.7 μm).

Experimental details (Feser et al. [66]): Circle symbols measured via a front-side TDTR experimental configuration using a $Nb_{0.43}V_{0.57}$ alloy deposited on a Quartz glass, where TDTR data is provided for TDTR offset scans along directions perpendicular and parallel to the Quartz crystal c-axis (f_{mod} = 1.11 MHz, τ_{d} = -20 ps, w_{Pump} = 1 μm).

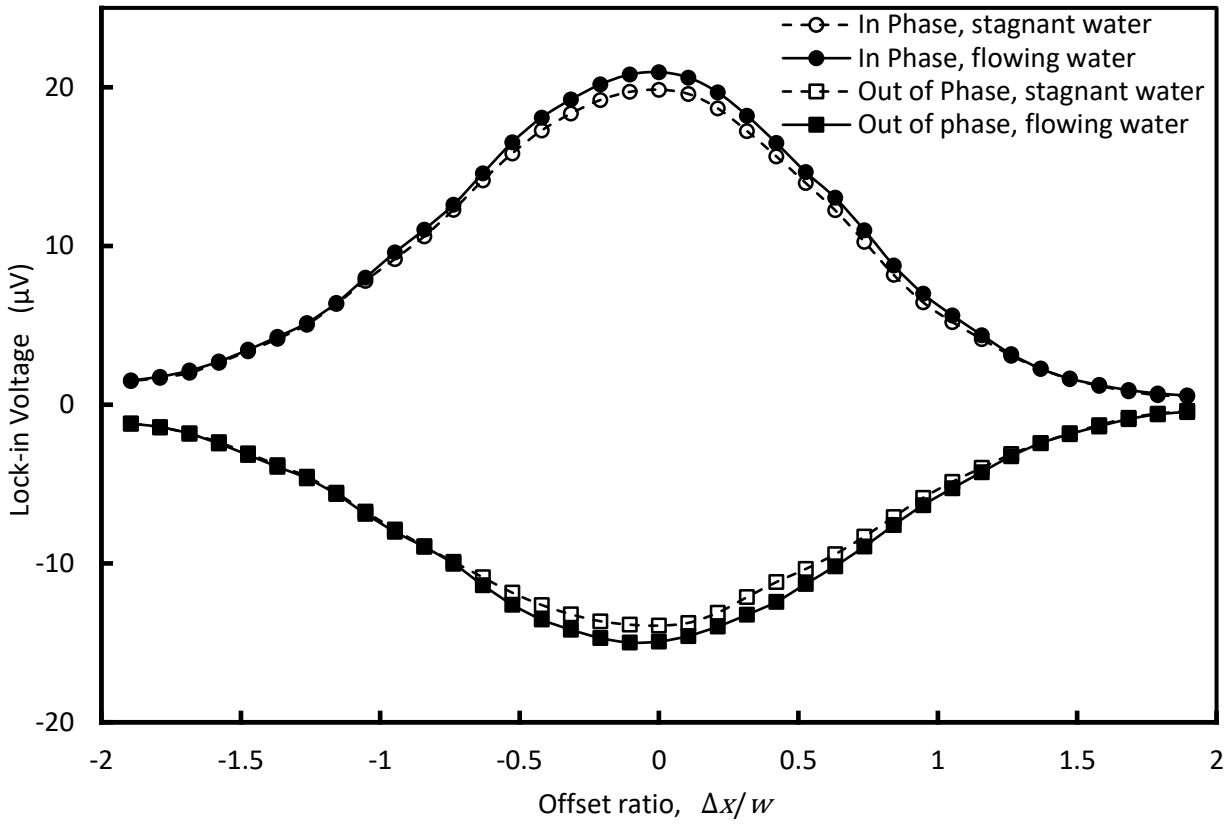

Figure A-6 In-phase (circle symbols) and out-of-phase (square symbols) components of measured TDTR signal as a function of pump-probe offset ratio for a $Nb_{0.5}V_{0.5}$ -coated FS substrate in thermal contact with stagnant (open symbols) and flowing (closed symbols) water in the microchannel.

Experimental details: $\mathrm{Re}_D = 1850$, $f_{\mathrm{mod}} = 962$ kHz, $P_{Pump} \approx 10.5$ mW, $P_{Probe} \approx 2.8$ mW, $w_{Pump} = 8.7$ μm, $w_{Probe} = 6.7$ μm.

Comments: The plot shows that both in-phase and out-of-phase voltage signals increase with water flow in the microchannel. However, we found that both the in-phase (V_{in}) and out-of-phase (V_{out}) voltages increased equally in magnitude with fluid flow (unlike our flow-induced TDTR results with Ti and Hf80 thin-films). Therefore, the TDTR ratio for this $Nb_{0.5}V_{0.5}$ thin-film (as a heater/thermometer) was not very sensitive to

changes in fluid flow. And while, we do observe anisotropic TDTR results with a $Nb_{0.5}V_{0.5}$ heater/thermometer, we are not sure how to interpret the measured data for HTC analysis.

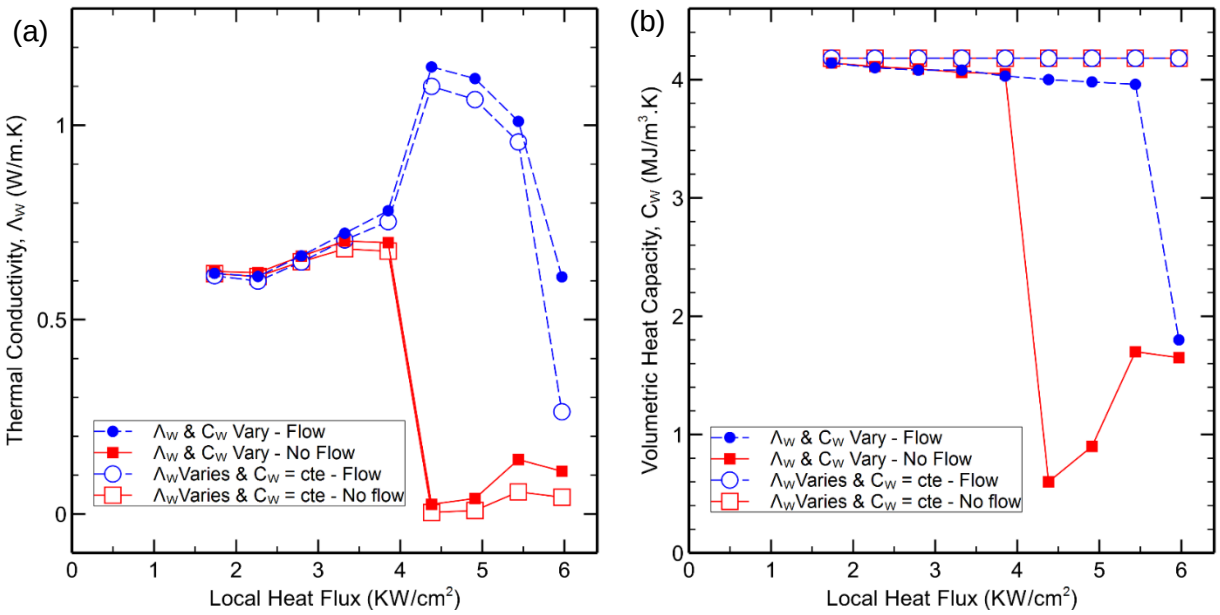

Figure A-7 Thermal conductivity (a) and volumetric heat capacity (b) of the fluid using two methods, variable Λ_w and constant C_w (open markers) and variable Λ_w and C_w (filled markers) for both stagnant (red squares) and flowing (blue circles) fluids.

APPENDIX B:

COPYRIGHT PERMISSION LETTERS

1) The following IEEE copyright/ credit notice should be placed prominently in the references: © [year of original publication] IEEE. Reprinted, with permission, from [author names, paper title, IEEE publication title, and month/year of publication]

2) Only the accepted version of an IEEE copyrighted paper can be used when posting the paper or your thesis on-line.

3) In placing the thesis on the author's university website, please display the following message in a prominent place on the website: In reference to IEEE copyrighted material which is used with permission in this thesis, the IEEE does not endorse any of [university/educational entity's name goes here]'s products or services. Internal or personal use of this material is permitted. If interested in reprinting/republishing IEEE copyrighted material for advertising or promotional purposes or for creating new collective works for resale or redistribution, please go to

http://www.ieee.org/publications_standards/publications/rights/rights_link.html to learn how to obtain a License from RightsLink.

If applicable, University Microfilms and/or ProQuest Library, or the Archives of Canada may supply single copies of the dissertation.

m.mehrvand

From: Beth Darchi <DarchiB@asme.org>
Sent: Thursday, June 15, 2017 10:55 AM
To: m.mehrvand
Subject: RE: copyright permission letter request

Dear Mr. Mehrvand,
It is our pleasure to grant you permission to use **all or any part of** the ASME paper "Probing the Local Heat Transfer Coefficient of Water-Cooled Microchannels using Time-domain Thermoreflectance," by Mehrdad Mehrvand and Shawn A. Putnam, Journal of Heat Transfer, 2017, cited in your letter for inclusion in a PhD dissertation to be published by University of Central Florida.

Permission is granted for the specific use as stated herein and does not permit further use of the materials without proper authorization. Proper attribution must be made to the author(s) of the materials. **Please note:** if any or all of the figures and/or Tables are of another source, permission should be granted from that outside source or include the reference of the original source. ASME does not grant permission for outside source material that may be referenced in the ASME works.

As is customary, we request that you ensure full acknowledgment of this material, the author(s), source and ASME as original publisher. Acknowledgment must be retained on all pages where figure is printed and distributed.

Many thanks for your interest in ASME publications.

Sincerely,

Beth Darchi
Publishing Administrator
ASME
2 Park Avenue
New York, NY 10016-5990
Tel 1.212.591.7700
darchib@asme.org

REFERENCES

[1] Waldrop, M. M., 2016, “The Chips Are down for Moore’s Law,” Nature, **530**(7589), pp. 144–147.

[2] Lienhard, J. H., and Khounsary, A. M., 1993, “Liquid Jet Impingement Cooling with Diamond Substrates for Extremely High Heat Flux Applications,” Proc. SPIE - Int. Soc. Opt. Eng., pp. 29–43.

[3] Won, Y., Cho, J., Agonafer, D., Asheghi, M., and Goodson, K. E., 2015, “Fundamental Cooling Limits for High Power Density Gallium Nitride Electronics,” IEEE Trans. Components, Packag. Manuf. Technol., **5**(6), pp. 737–744.

[4] Guenin, B., 2006, “Packaging Challenges For High Heat Flux Devices,” electronics-cooling [Online]. Available: https://www.electronics-cooling.com/2006/08/packaging-challenges-for-high-heat-flux-devices/.

[5] Semiconductor Industry Association, 2013, *International Technology Roadmap for Semiconductors (ITRS)*.

[6] Wang, Y., Qin, Z., Buehler, M. J., and Xu, Z., 2016, “Intercalated Water Layers Promote Thermal Dissipation at Bio–nano Interfaces,” Nat. Commun., **7**, p. 12854.

[7] Pop, E., 2010, “Energy Dissipation and Transport in Nanoscale Devices,” Nano Res., **3**(3), pp. 147–169.

[8] Cahill, D. G., Braun, P. V., Chen, G., Clarke, D. R., Fan, S., Goodson, K. E., Keblinski, P., King, W. P., Mahan, G. D., Majumdar, A., Maris, H. J., Phillpot, S. R., Pop, E., and Shi, L., 2014, “Nanoscale Thermal Transport. II. 2003-2012,” Appl. Phys. Rev., **1**(1).

[9] Ge, Z., Cahill, D. G., and Braun, P. V., 2006, “Thermal Conductance of Hydrophilic and Hydrophobic Interfaces,” Phys. Rev. Lett., **96**(18), pp. 1–4.

[10] Costescu, R. M., Wall, M. A., and Cahill, D. G., 2003, “Thermal Conductance of Epitaxial Interfaces,” Phys. Rev. B, **67**(5), p. 54302.

[11] Lyeo, H. K., and Cahill, D. G., 2006, “Thermal Conductance of Interfaces between Highly Dissimilar Materials,” Phys. Rev. B - Condens. Matter Mater. Phys., **73**(14).

[12] Lyeo, H. K., and Cahill, D. G., 2006, “Thermal Conductance of Interfaces,” Phys. Rev. B, **73**(14), p. 144301.

[13] Gundrum, B. C., Cahill, D. G., and Averback, R. S., 2005, “Thermal Conductance of Metal-Metal Interfaces,” Phys. Rev. B - Condens. Matter Mater. Phys., **72**(24).

[14] Hu, M., Keblinski, P., Wang, J. S., and Raravikar, N., 2008, “Interfacial Thermal Conductance between Silicon and a Vertical Carbon Nanotube,” J. Appl. Phys., **104**(8).

[15] Hamada, F. N., Rosenzweig, M., Kang, K., Pulver, S. R., Ghezzi, A., Jegla, T. J., and Garrity, P. A., 2008, “An Internal Thermal Sensor Controlling Temperature Preference in Drosophila,” Nature, **454**(7201), pp. 217–220.

[16] Garimella, S. V., 2006, “Advances in Mesoscale Thermal Management Technologies for Microelectronics,” Microelectronics J., **37**(11), pp. 1165–1185.

[17] Seletskiy, D. V., Melgaard, S. D., Bigotta, S., Di Lieto, A., Tonelli, M., and Sheik-Bahae, M., 2010, “Laser Cooling of Solids to Cryogenic Temperatures,” Nat. Photonics.

[18] Lu, L., Han, X., Li, J., Hua, J., and Ouyang, M., 2013, “A Review on the Key Issues for Lithium-Ion Battery Management in Electric Vehicles,” J. Power Sources, **226**, pp. 272–288.

[19] Chen, L., Yang, M., Xu, Y., Zhang, Z., Li, Z., and Zhang, F., 2016, “Effects of Cooling on Bending Process of Heavy Rail Steel After Hot Rolling,” Metallogr. Microstruct. Anal., **5**(3), pp. 196–206.

[20] Farshidianfar, M. H., Khajepour, A., and Gerlich, A., 2016, “Real-Time Control of Microstructure in Laser Additive Manufacturing,” Int. J. Adv. Manuf. Technol., **82**(5–8), pp. 1173–1186.

[21] Wu, Z., and Sundén, B., 2014, “On Further Enhancement of Single-Phase and Flow Boiling Heat Transfer in Micro/minichannels,” Renew. Sustain. Energy Rev., **40**, pp. 11–27.

[22] Asadi, M., Xie, G., and Sunden, B., 2014, “A Review of Heat Transfer and Pressure Drop Characteristics of Single and Two-Phase Microchannels,” Int. J. Heat Mass Transf., **79**, pp. 34–53.

[23] Kositanont, C., Putivisutisak, S., Tagawa, T., Yamada, H., and Assabumrungrat, S., 2014, “Multiphase Parallel Flow Stabilization in Curved Microchannel,” Chem. Eng. J., **253**, pp. 332–340.

[24] Khanikar, V., Mudawar, I., and Fisher, T., 2009, “Effects of Carbon Nanotube Coating on Flow Boiling in a Micro-Channel,” Int. J. Heat Mass Transf., **52**(15–16), pp. 3805–3817.

[25] Ujereh, S., Fisher, T., and Mudawar, I., 2007, “Effects of Carbon Nanotube Arrays on Nucleate Pool Boiling,” Int. J. Heat Mass Transf., **50**(19–20), pp. 4023–4038.

[26] Chu, K.-H., Soo Joung, Y., Enright, R., Buie, C. R., and Wang, E. N., 2013,

"Hierarchically Structured Surfaces for Boiling Critical Heat Flux Enhancement," Appl. Phys. Lett., **102**(15), p. 151602.

[27] Kim, J. H., You, S. M., and Choi, S. U. S., 2004, "Evaporative Spray Cooling of Plain and Microporous Coated Surfaces," Int. J. Heat Mass Transf., **47**(14–16), pp. 3307–3315.

[28] Chen, R.-H., Chow, L. C., and Navedo, J. E., 2002, "Effects of Spray Characteristics on Critical Heat Flux in Subcooled Water Spray Cooling," Int. J. Heat Mass Transf., **45**(19), pp. 4033–4043.

[29] Putra, N., Yanuar, and Iskandar, F. N., 2011, "Application of Nanofluids to a Heat Pipe Liquid-Block and the Thermoelectric Cooling of Electronic Equipment," Exp. Therm. Fluid Sci., **35**(7), pp. 1274–1281.

[30] Palko, J. W., Zhang, C., Wilbur, J. D., Dusseault, T. J., Asheghi, M., Goodson, K. E., and Santiago, J. G., 2015, "Approaching the Limits of Two-Phase Boiling Heat Transfer: High Heat Flux and Low Superheat," Appl. Phys. Lett., **107**(25).

[31] Sarafraz, M. M., and Hormozi, F., 2014, "Experimental Study on the Thermal Performance and Efficiency of a Copper Made Thermosyphon Heat Pipe Charged with Alumina–glycol Based Nanofluids," Powder Technol., **266**, pp. 378–387.

[32] Putnam, S. A., Briones, A. M., Byrd, L. W., Ervin, J. S., Hanchak, M. S., White, A., and Jones, J. G., 2012, "Microdroplet Evaporation on Superheated Surfaces," Int. J. Heat Mass Transf., **55**(21–22), pp. 5793–5807.

[33] Lin, S.-M., Liu, H.-F., Wang, W.-R., Lee, S. Y., Cheng, C.-Y., and Li, C.-Y., 2015, "Optimum Design and Heat Transfer Correlation Equation of a Mini Radiator with Jet Impingement Cooling," Appl. Therm. Eng., **89**, pp. 727–737.

[34] Kim, C.-B., Leng, C., Wang, X.-D., Wang, T.-H., and Yan, W.-M., 2015, "Effects of Slot-Jet Length on the Cooling Performance of Hybrid Microchannel/slot-Jet Module," Int. J. Heat Mass Transf., **89**, pp. 838–845.

[35] Zhao, Z., Peles, Y., and Jensen, M. K., 2013, "Water Jet Impingement Boiling from Structured-Porous Surfaces," Int. J. Heat Mass Transf., **63**, pp. 445–453.

[36] Karayiannis, T. G., and Mahmoud, M. M., 2016, "Flow Boiling in Microchannels: Fundamentals and Applications," Appl. Therm. Eng.

[37] Carey, V., 1992, "Liquid-Vapor Phase-Change Phenomena: An Introduction to the Themophysics of Vaporization and Condensation Processes in Heat Transfer Equipment," *Liquid-Vapor Phase-Change Phenomena: An Introduction to the Themophysics of Vaporization and Condensation Processes in Heat Transfer Equipment*, pp. 150–197.

[38] Kim, S.-M., and Mudawar, I., 2012, “Consolidated Method to Predicting Pressure Drop and Heat Transfer Coefficient for Both Subcooled and Saturated Flow Boiling in Micro-Channel Heat Sinks,” Int. J. Heat Mass Transf., **55**(13), pp. 3720–3731.

[39] Sung, M. K., and Mudawar, I., 2008, “Single-Phase and Two-Phase Hybrid Cooling Schemes for High-Heat-Flux Thermal Management of Defense Electronics,” *2008 11th IEEE Intersociety Conference on Thermal and Thermomechanical Phenomena in Electronic Systems, I-THERM*, pp. 121–131.

[40] Yang, J., Pais, M. R., and Chow, L. C., 1993, “High Heat Flux Spray Cooling,” pp. 29–40.

[41] Colgan, E. G., Furman, B., Gaynes, M., Graham, W. S., LaBianca, N. C., Magerlein, J. H., Polastre, R. J., Rothwell, M. B., Bezama, R. J., Choudhary, R., Marston, K. C., Toy, H., Wakil, J., Zitz, J. A., and Schmidt, R. R., 2007, “A Practical Implementation of Silicon Microchannel Coolers for High Power Chips,” IEEE Trans. Components Packag. Technol., **30**(2), pp. 218–225.

[42] Pasupuleti, T., and Kandlikar, S. G., 2009, “Cooling of Microelectronic Devices Packaged in a Single Chip Module Using Single Phase Refrigerant R-123,” Proc. ASME 2009 7th Int. Conf. Nanochannels, Microchannels Minichannels ICNMM2009-82262, pp. 1–5.

[43] Steinke, M. E., and Kandlikar, S. G., 2004, “An Experimental Investigation of Flow Boiling Characteristics of Water in Parallel Microchannels,” J. Heat Transfer, **126**(4), pp. 518–526.

[44] Zhu, Y., Antao, D. S., Chu, K.-H., Chen, S., Hendricks, T. J., Zhang, T., and Wang, E. N., 2016, “Surface Structure Enhanced Microchannel Flow Boiling,” J. Heat Transfer, **138**(9), pp. 91501–91513.

[45] Kim, S.-M., and Mudawar, I., 2013, “Universal Approach to Predicting Heat Transfer Coefficient for Condensing Mini/micro-Channel Flow,” Int. J. Heat Mass Transf., **56**(1), pp. 238–250.

[46] Browne, E. A., Michna, G. J., Jensen, M. K., and Peles, Y., 2010, “Microjet Array Single-Phase and Flow Boiling Heat Transfer with R134a,” Int. J. Heat Mass Transf., **53**(23–24), pp. 5027–5034.

[47] Rylatt, D. I., and O’Donovan, T. S., 2013, “Heat Transfer Enhancement to a Confined Impinging Synthetic Air Jet,” Appl. Therm. Eng., **51**(1–2), pp. 468–475.

[48] Chen, Y.-J., Li, Y.-Y., and Liu, Z.-H., 2015, “Experimental Study on the Stagnation Line Heat Transfer Characteristics with High-Velocity Free Slot Jet Impingement Boiling,” Int. J. Heat Mass Transf., **91**, pp. 282–292.

[49] Kim, J., 2007, “Spray Cooling Heat Transfer: The State of the Art,” Int. J. Heat Fluid

Flow, **28**(4), pp. 753–767.

[50] Qiu, L., Dubey, S., Choo, F. H., and Duan, F., 2015, “Recent Developments of Jet Impingement Nucleate Boiling,” Int. J. Heat Mass Transf., **89**, pp. 42–58.

[51] Liu, X., Gabour, L. A., and Lienhard J. H., V., 1993, “Stagnation-Point Heat Transfer During Impingement of Laminar Liquid Jets: Analysis Including Surface Tension,” J. Heat Transfer, **115**(1), pp. 99–105.

[52] Mitsutake, Y., and Monde, M., 2003, “Ultra High Critical Heat Flux During Forced Flow Boiling Heat Transfer With an Impinging Jet,” J. Heat Transfer, **125**(6), pp. 1038–1045.

[53] Kuo, C.-J., and Peles, Y., 2009, “Flow Boiling of Coolant (HFE-7000) Inside Structured and Plain Wall Microchannels,” J. Heat Transfer, **131**(12), p. 121011.

[54] Horacek, B., Kiger, K. T., and Kim, J., 2005, “Single Nozzle Spray Cooling Heat Transfer Mechanisms,” Int. J. Heat Mass Transf., **48**(8), pp. 1425–1438.

[55] Rainey, K. N., You, S. M., and Lee, S., 2003, “Effect of Pressure, Subcooling, and Dissolved Gas on Pool Boiling Heat Transfer from Microporous, Square Pin-Finned Surfaces in FC-72,” Int. J. Heat Mass Transf., **46**(1), pp. 23–35.

[56] Steinke, M. E., and Kandlikar, S. G., 2004, “Control and Effect of Dissolved Air in Water during Flow Boiling in Microchannels,” Int. J. Heat Mass Transf., **47**(8–9), pp. 1925–1935.

[57] Horacek, B., Kim, J., and Kiger, K. T. K. T., 2004, “Spray Cooling Using Multiple Nozzles: Visualization and Wall Heat Transfer Measurements,” IEEE Trans. Device Mater. Reliab., **4**(4), pp. 614–625.

[58] Putnam, S. A., Briones, A. M., Ervin, J. S., Hanchak, M. S., Byrd, L. W., and Jones, J. G., 2012, “Interfacial Heat Transfer During Microdroplet Evaporation on a Laser Heated Surface,” Int. J. Heat Mass Transf., **55**(23–24), pp. 6307–6320.

[59] Bigham, S., and Moghaddam, S., 2015, “Microscale Study of Mechanisms of Heat Transfer during Flow Boiling in a Microchannel,” Int. J. Heat Mass Transf., **88**, pp. 111–121.

[60] Buongiorno, J., Cahill, D. G., Hidrovo, C. H., Moghaddam, S., Schmidt, A. J., and Shi, L., 2014, “Micro- and Nanoscale Measurement Methods for Phase Change Heat Transfer on Planar and Structured Surfaces,” Nanoscale Microscale Thermophys. Eng., **18**(3), pp. 270–287.

[61] Plawsky, J. L., Fedorov, A. G., Garimella, S. V., Ma, H. B., Maroo, S. C., Chen, L., and Nam, Y., 2014, “Nano- and Microstructures for Thin-Film Evaporation—A Review,” Nanoscale Microscale Thermophys. Eng., **18**(3), pp. 251–269.

[62] Cahill, D. G., 2004, “Analysis of Heat Flow in Layered Structures for Time-Domain Thermoreflectance,” Rev. Sci. Instrum., **75**(12), pp. 5119–5122.

[63] Kang, K., Koh, Y. K., Chiritescu, C., Zheng, X., and Cahill, D. G., 2008, “Two-Tint Pump-Probe Measurements Using a Femtosecond Laser Oscillator and Sharp-Edged Optical Filters,” Rev. Sci. Instrum., **79**(11), pp. 1–5.

[64] Schmidt, A. J., Chiesa, M., Chen, X., and Chen, G., 2008, “An Optical Pump-Probe Technique for Measuring the Thermal Conductivity of Liquids.,” Rev. Sci. Instrum., **79**(6), p. 064902 1-5.

[65] Feser, J. P., and Cahill, D. G., 2012, “Probing Anisotropic Heat Transport Using Time-Domain Thermoreflectance with Offset Laser Spots,” Rev. Sci. Instrum., **83**(10), p. 104901.

[66] Feser, J. P., Liu, J., and Cahill, D. G., 2014, “Pump-Probe Measurements of the Thermal Conductivity Tensor for Materials Lacking in-Plane Symmetry.,” Rev. Sci. Instrum., **85**(10), p. 104903.

[67] Childs, P. R. N., 2016, “Chapter 1 Nanoscale Thermometry and Temperature Measurement,” *Thermometry at the Nanoscale: Techniques and Selected Applications*, The Royal Society of Chemistry, pp. 1–22.

[68] Kang, K., Koh, Y. K., Chiritescu, C., Zheng, X., and Cahill, D. G., 2008, “Two-Tint Pump-Probe Measurements Using a Femtosecond Laser Oscillator and Sharp-Edged Optical Filters,” Rev. Sci. Instrum., **79**(11).

[69] English, T. S., Phinney, L. M., Hopkins, P. E., and Serrano, J. R., 2013, “Mean Free Path Effects on the Experimentally Measured Thermal Conductivity of Single-Crystal Silicon Microbridges,” J. Heat Transfer, **135**(September 2013), p. 91103.

[70] Koh, Y. K., Singer, S. L., Kim, W., Zide, J. M. O., Lu, H., Cahill, D. G., Majumdar, A., and Gossard, A. C., 2009, “Comparison of the 3?? Method and Time-Domain Thermoreflectance for Measurements of the Cross-Plane Thermal Conductivity of Epitaxial Semiconductors,” J. Appl. Phys., **105**(5).

[71] Xu, L. Y., and Cheng, Y. F., 2009, “Effect of Fluid Hydrodynamics on Flow-Assisted Corrosion of Aluminum Alloy in Ethylene Glycol–water Solution Studied by a Microelectrode Technique,” Corros. Sci., **51**(10), pp. 2330–2335.

[72] Chen, X., Tian, W., Li, S., Yu, M., and Liu, J., 2015, “Effect of Temperature on Corrosion Behavior of 3003 Aluminum Alloy in Ethylene Glycol–water Solution,” Chinese J. Aeronaut.

[73] Bozorgi, P., and Fleischman, G., 2014, “Ultra-Thin Titanium Based Thermal Solution for Electronic Applications,” Electron. Cool. Mag., p. 4 [Online]. Available: http://www.electronics-cooling.com/2014/02/ultra-thin-titanium-based-thermal-

solution-electronic-applications/.

[74] Incropera, F. P., DeWitt, D. P., Bergman, T. L., and Lavine, A. S., 2007, *Fundamentals of Heat and Mass Transfer*.

[75] Lee, P. S., Garimella, S. V., and Liu, D., 2005, “Investigation of Heat Transfer in Rectangular Microchannels,” Int. J. Heat Mass Transf., **48**(9), pp. 1688–1704.

[76] Lee, P.-S., and Garimella, S. V., 2006, “Thermally Developing Flow and Heat Transfer in Rectangular Microchannels of Different Aspect Ratios,” Int. J. Heat Mass Transf., **49**(17–18), pp. 3060–3067.

[77] Gad-el-hak, M., 1999, “The Fluid Mechanics of Microdevices — The Freeman Scholar Lecture,” J. Fluids Eng., **121**(March), pp. 5–33.

[78] Incropera, F. P., DeWitt, D. P., Bergman, T. L., and Lavine, A. S., 2007, *Fundamentals of Heat and Mass Transfer*, John Wiley & Sons.

[79] Shabany, Y., 2009, *Heat Transfer: Thermal Management of Electronics*, CRC Press.

[80] Schmidt, A. J., Cheaito, R., and Chiesa, M., 2010, “Characterization of Thin Metal Films via Frequency-Domain Thermoreflectance,” J. Appl. Phys., **107**(2), p. 24908.

[81] Johnson, J. A., Maznev, A. A., Cuffe, J., Eliason, J. K., Minnich, A. J., Kehoe, T., Torres, C. M. S., Chen, G., and Nelson, K. A., 2013, “Direct Measurement of Room-Temperature Nondiffusive Thermal Transport over Micron Distances in a Silicon Membrane,” Phys. Rev. Lett., **110**(2).

[82] Schmidt, A. J., Chen, X., and Chen, G., 2008, “Pulse Accumulation, Radial Heat Conduction, and Anisotropic Thermal Conductivity in Pump-Probe Transient Thermoreflectance,” Rev. Sci. Instrum., **79**(11), p. 114902.

[83] E. Marin, L. S. Vaca-Oyola, O. D.-V., 2016, “On Thermal Waves’ Velocity: Some Open Questions in Thermal Waves’ Physics,” Mex. F´ısica, **E**(62), pp. 1–4.

[84] Shah, R. K., and London, A. L., 1978, *Laminar Flow Forced Convection in Ducts*.

[85] Muzychka, Y. S., and Yovanovich, M. M., 2004, “Laminar Forced Convection Heat Transfer in the Combined Entry Region of Non-Circular Ducts,” J. Heat Transfer, **126**(1), pp. 54–61.

[86] Mansoor, M. M., Wong, K.-C., and Siddique, M., 2012, “Numerical Investigation of Fluid Flow and Heat Transfer under High Heat Flux Using Rectangular Micro-Channels,” Int. Commun. Heat Mass Transf., **39**(2), pp. 291–297.

[87] Stephan, K., and Preußer, P., 1979, “Wärmeübergang Und Maximale

Wärmestromdichte Beim Behältersieden Binärer Und Ternärer Flüssigkeitsgemische," Chemie Ing. Tech., **51**(1), p. 37.

[88] M. Thirumaleshwar, 2006, *Fundamentals of Heat and Mass Transfer*, Pearson Education, New Dehli.

[89] Carslow, H. S., Jaeger, J. C., and Morral, J. E., 1986, *Conduction of Heat in Solids, Second Edition*.

[90] Koh, Y. K., and Cahill, D. G., 2007, "Frequency Dependence of the Thermal Conductivity of Semiconductor Alloys," Phys. Rev. B, **76**(7), p. 75207 1-5.

[91] Kandlikar, S. G., 2001, "Critical Heat Flux in Subcooled Flow Boiling-an Assessment of Current Understanding and Future Directions for Research," Multiph. Sci. Technol., **13**(3–4).

[92] Maddox, D. E., and Mudawar, I., 1989, "Single- and Two-Phase Convective Heat Transfer From Smooth and Enhanced Microelectronic Heat Sources in a Rectangular Channel," J. Heat Transfer, **111**(4), pp. 1045–1052.

[93] Incropera, F. P., Kerby, J. S., Moffatt, D. F., and Ramadhyani, S., 1986, "Convection Heat Transfer from Discrete Heat Sources in a Rectangular Channel," Int. J. Heat Mass Transf., **29**(7), pp. 1051–1058.

[94] Dhir, V. K., 2003, "Phase Change Heat Transfer -- A Perspective for the Future," Rohsenow Symp. Futur. Trends Heat Transf., pp. 1–6.

[95] Cho, J., and Goodson, K. E., 2015, "Thermal Transport: Cool Electronics," Nat. Mater., **14**(2), pp. 136–137.

[96] Suzuki, K., Yuki, K., and Mochizuki, M., 2011, "Application of Boiling Heat Transfer to High-Heat-Flux Cooling Technology in Power Electronics," pp. 127–133.

[97] Marcinichen, J. B., Olivier, J. A., and Thome, J. R., 2012, "On-Chip Two-Phase Cooling of Datacenters: Cooling System and Energy Recovery Evaluation," *Applied Thermal Engineering*, pp. 36–51.

[98] Szczukiewicz, S., Lamaison, N., Marcinichen, J. B., Thome, J. R., and Beucher, P. J., 2015, "Passive Thermosyphon Cooling System for High Heat Flux Servers," *ASME 2015 International Technical Conference and Exhibition on Packaging and Integration of Electronic and Photonic Microsystems, InterPACK 2015, Collocated with the ASME 2015 13th International Conference on Nanochannels, Microchannels, and Minichannels*.

[99] Puscasu, O., Monfray, S., Maître, C., Cottinet, P. J., Rapisarda, D., Savelli, G., Gaillard, F., Ricotti, G., Ancey, P., Boeuf, F., Guyomar, D., and Skotnicki, T., 2014, "A Disruptive Technology for Thermal to Electrical Energy Conversion,"

Microelectronics J., **45**(5), pp. 554–558.

[100] Sung, M. K., and Mudawar, I., 2009, “Single-Phase and Two-Phase Hybrid Cooling Schemes for High-Heat-Flux Thermal Management of Defense Electronics,” J. Electron. Packag., **131**(2), p. 21013.

[101] Bigham, S., and Moghaddam, S., 2015, “Role of Bubble Growth Dynamics on Microscale Heat Transfer Events in Microchannel Flow Boiling Process,” Appl. Phys. Lett., **107**(24).

[102] Li, W., Yang, F., Alam, T., Khan, J., and Li, C., 2015, “Experimental and Theoretical Studies of Critical Heat Flux of Flow Boiling in Microchannels with Microbubble-Excited High-Frequency Two-Phase Oscillations,” Int. J. Heat Mass Transf., **88**, pp. 368–378.

[103] Rao, S. R., and Peles, Y., 2015, “Spatiotemporally Resolved Heat Transfer Measurements for Flow Boiling in Microchannels,” Int. J. Heat Mass Transf., **89**, pp. 482–493.

[104] Saha, S. K., 2016, *Editorial by Sujoy Kumar Saha*, Elsevier.

[105] Buongiorno, J., 2010, “Notes On Two-Phase Flow, Boiling Heat Transfer, And Boiling Crisis In PWRs And BWRs,” MIT OpenCourseWare MIT Dep. Nucl. Sci. Eng. - 22.06 Eng. Nucl. Syst., pp. 1–34.

[106] Yu, X., Woodcock, C., Wang, Y., Plawsky, J. L., and Peles, Y., 2017, “Enhanced Subcooled Flow Boiling Heat Transfer in Microchannel with Piranha Pin Fin,” J. Heat Transfer.

[107] Betz, A. R., Jenkins, J., Kim, C. J., and Attinger, D., 2013, “Boiling Heat Transfer on Superhydrophilic, Superhydrophobic, and Superbiphilic Surfaces,” Int. J. Heat Mass Transf., **57**(2), pp. 733–741.

[108] Rao, S. R., Houshmand, F., and Peles, Y., 2014, “Transient Flow Boiling Heat-Transfer Measurements in Microdomains,” Int. J. Heat Mass Transf., **76**, pp. 317–329.

[109] Nam, Y., Wu, J., Warrier, G. R., and Ju, Y. S., 2009, “Experimental and Numerical Study of Single Bubble Dynamics on a Hydrophobic Surface,” J. Heat Transfer, **131**(12), p. 121004.

[110] Vafaei, S., and Borca-Tasciuc, T., 2014, “Role of Nanoparticles on Nanofluid Boiling Phenomenon: Nanoparticle Deposition,” Chem. Eng. Res. Des., **92**(5), pp. 842–856.

[111] Dhillon, N. S., Buongiorno, J., and Varanasi, K. K., 2015, “Critical Heat Flux Maxima during Boiling Crisis on Textured Surfaces,” Nat. Commun., **6**, p. 8247.

[112] Cho, H. J., Preston, D. J., Zhu, Y., and Wang, E. N., 2016, “Nanoengineered Materials for Liquid–vapour Phase-Change Heat Transfer,” Nat. Rev. Mater., **2**, p. 16092.

[113] Cho, H. J., Mizerak, J. P., and Wang, E. N., 2015, “Turning Bubbles on and off during Boiling Using Charged Surfactants.,” Nat. Commun., **6**(May), p. 8599.

[114] Dhillon, N. S., Buongiorno, J., and Varanasi, K. K., 2015, “Critical Heat Flux Maxima during Boiling Crisis on Textured Surfaces,” Nat. Commun., **6**, p. 8247.

[115] Nasarek, R., 2010, “Temperature Field Measurements with High Spatial and Temporal Resolution Using Liquid Crystal Thermography and Laser Induced Fluorescence,” **PhD**.

[116] Duan, X., Phillips, B., McKrell, T., and Buongiorno, J., 2013, “Synchronized High-Speed Video, Infrared Thermometry, and Particle Image Velocimetry Data for Validation of Interface-Tracking Simulations of Nucleate Boiling Phenomena,” Exp. Heat Transf., **26**(2–3), pp. 169–197.

[117] Kim, H., Park, Y., and Buongiorno, J., 2013, “Measurement of Wetted Area Fraction in Subcooled Pool Boiling of Water Using Infrared Thermography,” Nucl. Eng. Des., **264**, pp. 103–110.

[118] Mehrvand, M., and Putnam, S. A., 2016, “Heat Transfer Coefficient Measurements in the Thermal Boundary Layer of Microchannel Heat Sinks,” 2016 15th IEEE Intersoc. Conf. Therm. Thermomechanical Phenom. Electron. Syst., pp. 487–494.

[119] Mehrvand, M., and Putnam, S. A., 2017, “Probing the Local Heat Transfer Coefficient of Water-Cooled Microchannels Using Time-Domain Thermoreflectance,” J. Heat Transfer.

[120] Leong, K. C., Ho, J. Y., and Wong, K. K., 2017, “A Critical Review of Pool and Flow Boiling Heat Transfer of Dielectric Fluids on Enhanced Surfaces,” Appl. Therm. Eng., **112**, pp. 999–1019.

[121] Buchholz, M., Auracher, H., Lüttich, T., and Marquardt, W., 2006, “A Study of Local Heat Transfer Mechanisms along the Entire Boiling Curve by Means of Microsensors,” Int. J. Therm. Sci., **45**(3), pp. 269–283.

[122] Henry, C. D., and Kim, J., 2004, “A Study of the Effects of Heater Size , Subcooling , and Gravity Level on Pool Boiling Heat Transfer,” **25**, pp. 262–273.

[123] Stephan, P., and Hammer, J., 1994, “A New Model for Nucleate Boiling Heat Transfer,” Heat Mass Transf. Stoffuebertragung, **30**(2), pp. 119–125.

[124] Yang, F., Schultz, M., Parida, P., Colgan, E., Polastre, R., Dang, B., Tsang, C., Gaynes, M., Knickerbocker, J., and Chainer, T., 2015, “Local Measurements of

Flow Boiling Heat Transfer on Hot Spots in 3D Compatible Radial Microchannels,” (56901), p. V003T10A006.